Preliminary study of multiplicity dependence of light vector meson production at forward rapidity in pp collisions at $\sqrt{s}$ = 13 TeV

Graduate School of Science, Hiroshima Univerisity
Department of Physical Science
Experimental Quark Physics Laboratory
M175576

Yuji Kawamoto

Supervisor : Associate Professor Kenta Shigaki
Chief examiner : Associate Professor Kenta Shigaki
Vice-Examiner : Associate Professor Tsunefumi Mizuno

8th. February. 2019

Abstract

It is predicted that quarks and gluons are deconfined at a high temperature and high energy density. Such state, called Quark-Gluon Plasma (QGP) is reached in high-energy heavy-ion collisions in the laboratory. When QGP is formed in heavy-ion collisions, strange quark pairs are generated mainly through the gluon-gluon interaction. Therefore, strange hadrons are enhanced relative to the situation of no QGP formation, and it is suggested as one of the signal of QGP. Moreover, similar enhancement of $\mathrm{K^0_S}$, Λ, Ξ, Ω is recently observed in high-multiplicity events in pp collisions, where no enhancement was expected at LHC. One possible scenario is that the QGP also forms in high-multiplicity events in pp collisions. Production of ϕ meson, whose quark content is $s\bar{s}$, gives insight into such an effect in high-multiplicity event.

The multiplicity dependence of light vector meson production in pp collisions at $\sqrt{s} = 13$ TeV is measure with ALICE. The light vector mesons are measured a $-4 < y < -2.5$ via the dimuon channel. The light vector meson signals are extracted by subtracting the uncorrelated background by the like-sign method, and the correlated background by fitting with empirical functions. The multiplicity is estimated from number of tracklets in Silicon Pixel Detector (SPD). To evaluate the enhancement of ϕ meson, the ratio of the self-normalized yields of ϕ and ω meson, constituted by u and d quarks, is calculated in each multiplicity class. This ratio is found to be consistent to the constant. The trend seen at $p_T < 1$ GeV/c might however indicate thermal strangeness production.

Contents

List of Figures

List of Tables

1 Introduction

1.1 Quantum Chromodynamics (QCD)

QCD describes the strong interaction between quarks and gluons. QCD is characteristic for its properties of asymptotic freedom and color charge confinement. In QCD, quarks and gluons have not only electric charge but also color charge (red, green, blue), analogically corresponding to a set of primary colors. Therefore, gluons interact with theirselves (Fig.1) and it is the important difference between QCD and Quantum Electrodynamics (QED). This leads to the phenomenon called asymptotic freedom, where QCD coupling constant α_s decrease with increasing momentum transfer Q^2 as expressed below.

$$\alpha_s(Q^2) \propto \frac{1}{\ln(\mathrm{Q}^2/\Lambda^2_{\mathrm{QCD}})} \tag{1}$$

Λ^2_{QCD} is QCD momentum scale parameter, determined from experiments. Asymptotic freedom describes the fact that an isolated color charged or fractional charged particle has never been observed. Color charged particles are confined in the matter because color neutral(white) particles never generate color fields, therefore white is energetically favorable.

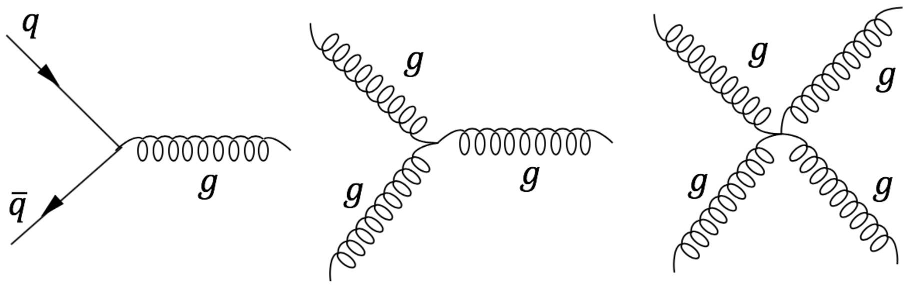

Figure 1: Vertices of QCD Feynman diagram

1.2 Quark-Gluon Plasma(QGP)

Quarks and gluons are confined in hadron as described in the previous section. However, under high enough temperature or density environment, α_s becomes small. This deconfined state is called QGP and such state is assumed to exist in the early universe. From lattice QCD calculation(Fig.2), critical temperature T_c between hadronic state and deconfined state is predicted to be $\mathrm{T}_c \approx 160$ MeV. In Fig.2, the abrupt increase of energy density around 160 MeV is seen and this shows phase shift to another state.

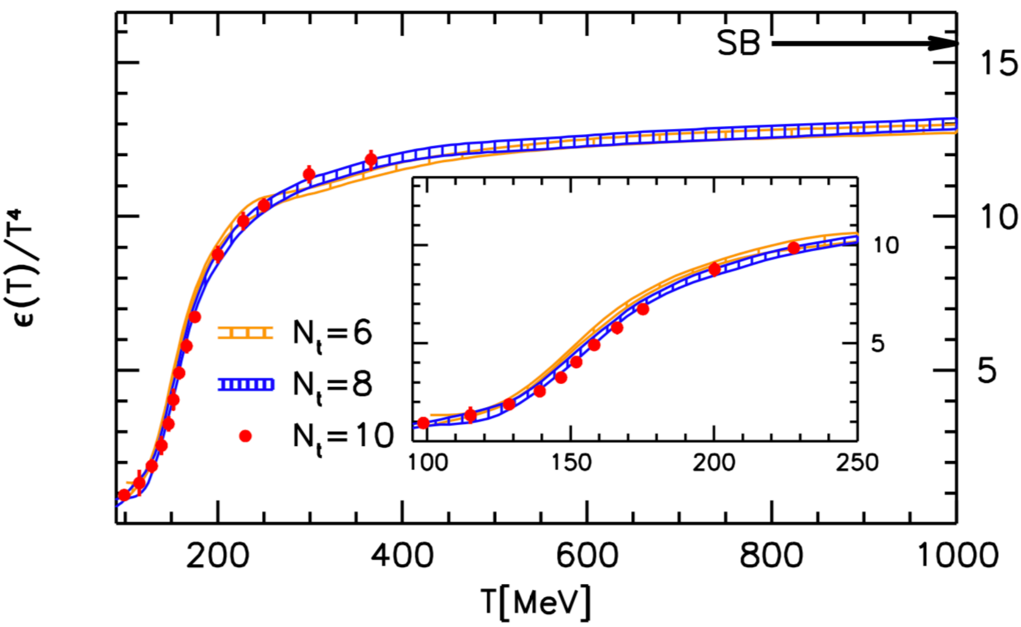

Figure 2: Energy density of quark-gluon field normalized by T^4 in finite temperature from lattice QCD calculation[7].

1.3 High energy heavy ion collision

High energy heavy ion collision is the unique way to reach the QGP state in a laboratory.

Accelerated nucleon

The nuclei are accelerated to almost the speed of light. Their shape is apparently modified like a disk due to Lorentz contraction. Because of the uncertainty principle, the thickness of this disk along the beam direction is about 1 fm.

Initial state

When the nuclei collide, partons in the nuclei scatter each other, and high energy density region appears within the passing nuclei. Such a process produces heavy quarks and jets.

QGP state

High energy density induces parton generation, and the system reaches the thermal equilibrium called QGP. It is known that the expansion of the system is well described with the hydrodynamics.

Hadronization

Just after the thermalization, the system starts cooling, expanding and hadronizing. Hadronization is modelized in two steps, chemical freeze out and kinematical freeze out. Because of the different cross sections of inelastic and elastic scattering of hadron species, chemical freeze out, which fixes the ratios of hadrons, is earlier than kinematical freeze out.

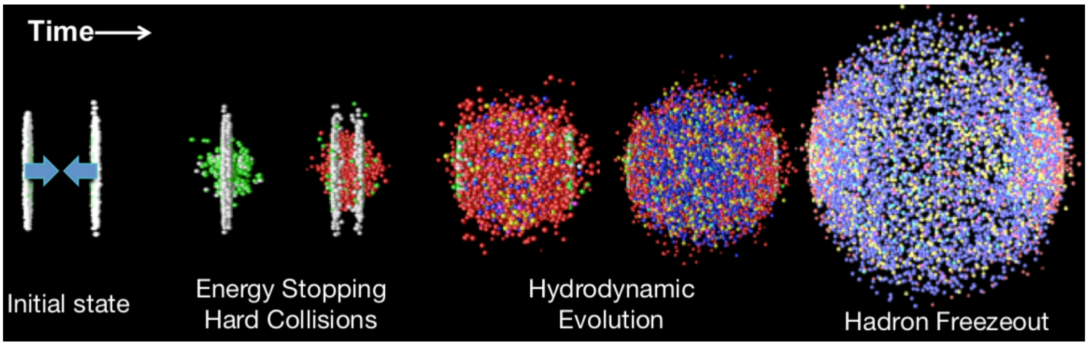

Figure 3: Schematic view of time evolution in a heavy ion collision [2].

1.4 Strangeness enhancement

The enhancement of strange hadrons relative to pp collisions with AA collisions is suggested as a signal of QGP in [3] for the first time. In QGP, $s\bar{s}$ is mainly produced by gluon fusion $gg \rightarrow s\bar{s}$ because of high gluon density. This is lower energy threshold process compared to the hadronic strangeness production process, therefore strange hadrons are enhanced in AA collisions. In hadron reaction, $\mathrm{N} + \mathrm{N} \rightarrow \mathrm{N} + \Lambda + \mathrm{K}$ for example, the energy threshold is about 660 MeV. In parton reactions, the energy threshold is about $2m_s \approx 300$ MeV.
In the Super Proton Synchrotron (SPS), fixed target experiment at CERN, saturation of enhancement relative to p-Pb collisions at 158 A GeV/c and a hierarchy depending on the strangeness content was found in hyperon production as a function of $\langle \mathrm{N}_{\mathrm{part}} \rangle$ in Pb-Pb collisions at 158 A GeV/c by WA97 experiment[4]. This enhancement is saturated at high $\langle \mathrm{N}_{\mathrm{part}} \rangle$ and this feature can be understood on the canonical suppression (CS) [5].

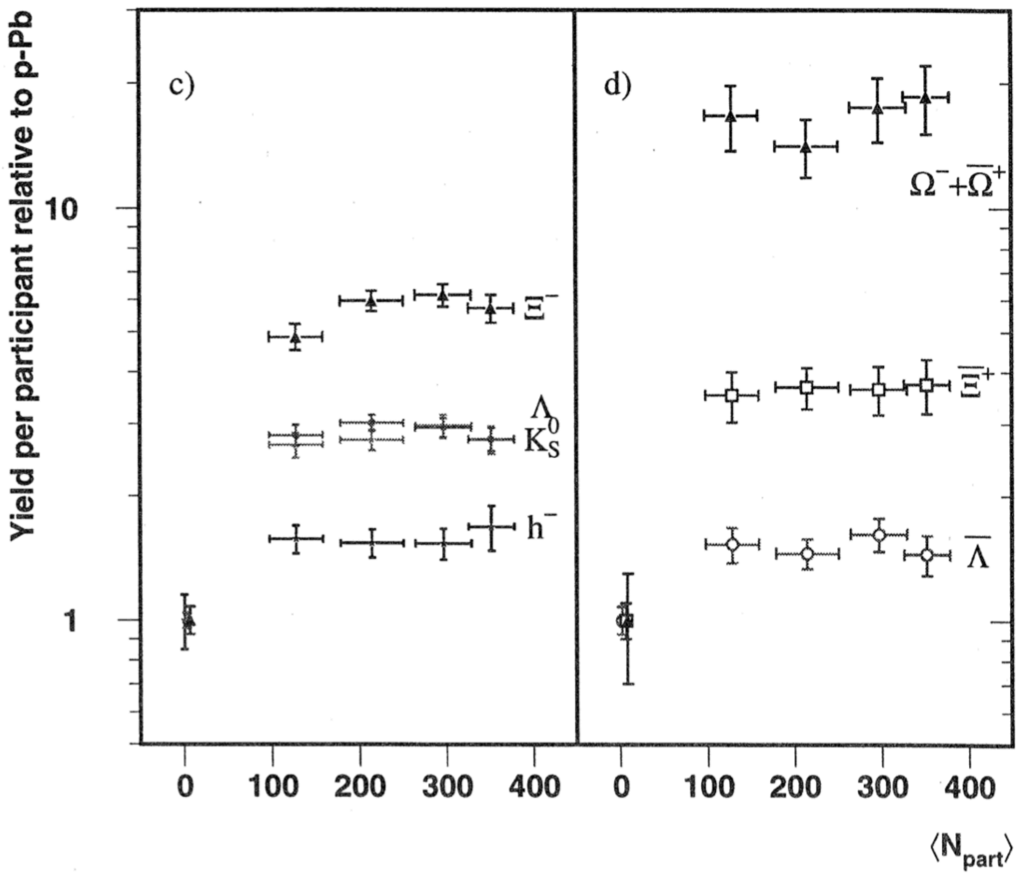

Figure 4: Yields of strange hadrons and negative charged hadrons in PbPb collisions at 158 A GeV/c relative to pPb collisions at 158 A GeV/c as a function of the number of participants.[4]

1.4.1 Canonical suppression

Considering AA system, the Grand Canonical formulation (GC) where strangeness quantum number can be implemented as the chemical potential is used. The GC formulation well describes the hadron yields over a wide beam energy range [6]. However, in small systems with small multiplicities like pp to pA collisions, conservation of strangeness must be implemented explicitly and this is the Canonical formulation (C).

For a particle with strangeness $s = 0, \pm1, \pm2, \pm3$, thermal particle density of a particle species i with strangeness s in a gas of total strangeness $= 0$ is expressed as [7]

$$n_i^C = \frac{1}{V}\frac{Z_i^1}{Z_{S=0}^C}\sum_{n=-\infty}^{\infty}\sum_{p=-\infty}^{\infty} a_3^p a_2^n a_1^{-2n-3p-s} I_n(x_2) I_p(x_3) I_{-2n-3p-s}(x_1) \tag{2}$$

where V is the volume parameter, assuming the size of nuclei or nucleon, and

$$a_i = \sqrt{S_i/S_{-i}} \tag{3}$$

$$x_i = 2\sqrt{S_i S_{-i}} \propto V \tag{4}$$

$$Z_{S=0}^{C} = \sum_{n=-\infty}^{\infty} \sum_{p=-\infty}^{\infty} a_3^p a_2^n a_1^{-2n-3p} I_n(x_2) I_p(x_3) I_{-2n-3p}(x_1). \tag{5}$$

I is modified Bessel function, and $I_s = I_{-s}$. $S_i = \sum_k Z_k^1$ is the summation of all partition function for particles same strangeness as i. The one-particle partition function is given by

$$Z_k^1 \equiv V \frac{g_k}{2\pi^2} m_k^2 T K_2(\frac{m_k}{T}) \exp(B_k \mu_B + Q_k \mu_Q) \tag{6}$$

where m_k is the mass of a particle, g_k is the spin-isospin degeneracy factor, B_k is the carrying baryon number, Q_k is the electric charge, μ_B, μ_Q are the corresponding chemical potential. For small x_1, we can express n_i^C as

$$n_i^C \simeq \frac{Z_i^1}{V} \frac{(S_1)^s}{(S_{+1} S_{-1})^{s/2}} \frac{I_s(x_1)}{I_0(x_1)} \tag{7}$$

and the canonical suppression factor is defined as

$$F_{CSs} = \frac{I_s(x_1)}{I_0(x_1)}. \tag{8}$$

The strangeness of particle is seen in the suppression factor, and for small x_1, $F_{CSs} \sim (x_1/2)^s$. In case of kaons for instance, n_{kaon}^C is linearly dependent on the volume V if x_1 is small. For hidden strange particles like ϕ meson, it is not suppressed because $F_{CSs} = 1$. This approach successfully describes the suppressed strangeness production in small collision systems, because the strict conservation of quantum numbers reduces the volume of particle production, so-called the canonical suppression (CS) [5].

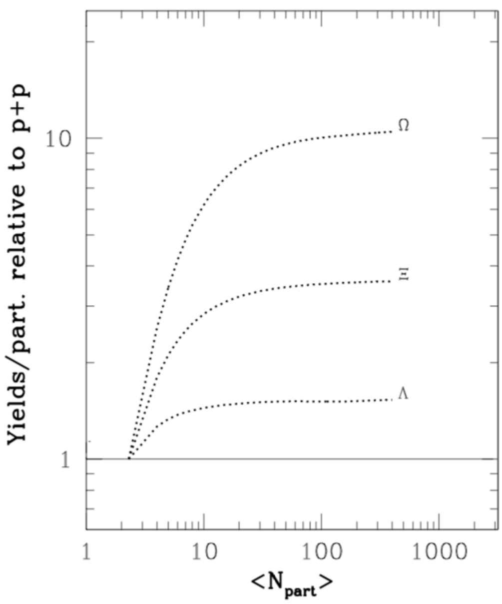

(a) $\langle \mathrm{N_{part}} \rangle$ dependence of relative yields/participants of strange hadrons in central pp to PbPb collisions at fixed energy $\sqrt{s} = 130$ GeV[5].

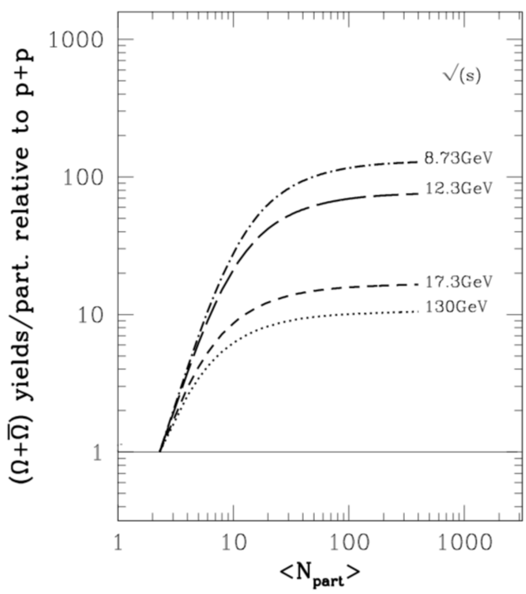

(b) $\langle \mathrm{N_{part}} \rangle$ dependence of relative yields/participants of $(\Omega + \bar{\Omega})$ in central pp to PbPb collisions at different collision energies[5].

1.5 Phenomenology in small systems

In recent years, two particle angular correlation structure for charged particles, called "ridge" and mass ordering of v_2 are observed in high-multiplicity pp collisions [8][9]. Furthermore, enhancements (shown in Fig.6) and their mass dependences of strange hadrons are observed at high-multiplicity events in $\sqrt{s}$ = 7 TeV pp collisions [10]. These effects are considered as typical of heavy-ion collisions, where QGP is formed.

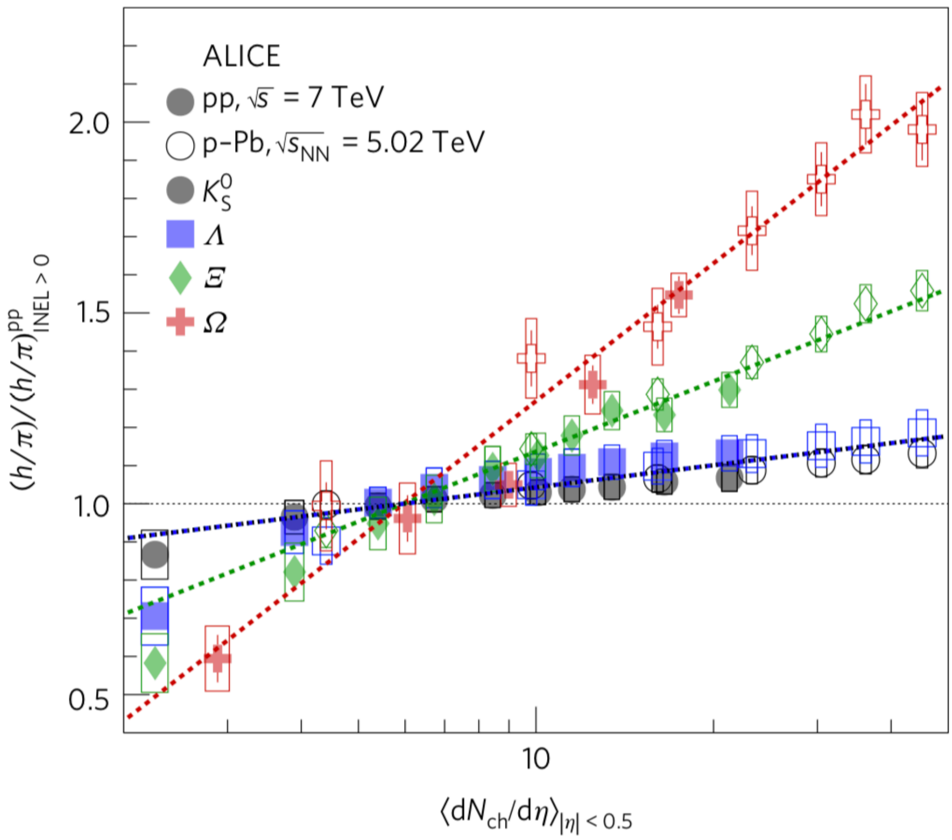

Figure 6: Strange hadrons yield ratios to pions normalized to the inclusive multiplicity value[10].

1.6 Motivation

As shown above, multiplicity dependence of strange hadrons is observed in pp collisions, which may indicate the QGP-like phenomenon in small systems. However, multiplicity dependence of ϕ meson has not yet been reported. According to the CS approach calculation at LHC energies[11], multiplicity dependence of yield ratio of ϕ meson and pions normalized by high-multiplicity limit is flat, unlike other strange hadrons and the data from pPb and PbPb collisions as shown in Fig.7. This fact indicates that ϕ meson is not canonically suppressed. Hence, ϕ meson could be sensitive for production mechanisms other than CS, like thermal $s\bar{s}$ production for instance.

In this study, ϕ and ω meson is used to estimate the enhanced production of strangeness. They are both measured via the "clean" dimuon channel, and we can compare mesons with strange quarks and without them in the same mass range.

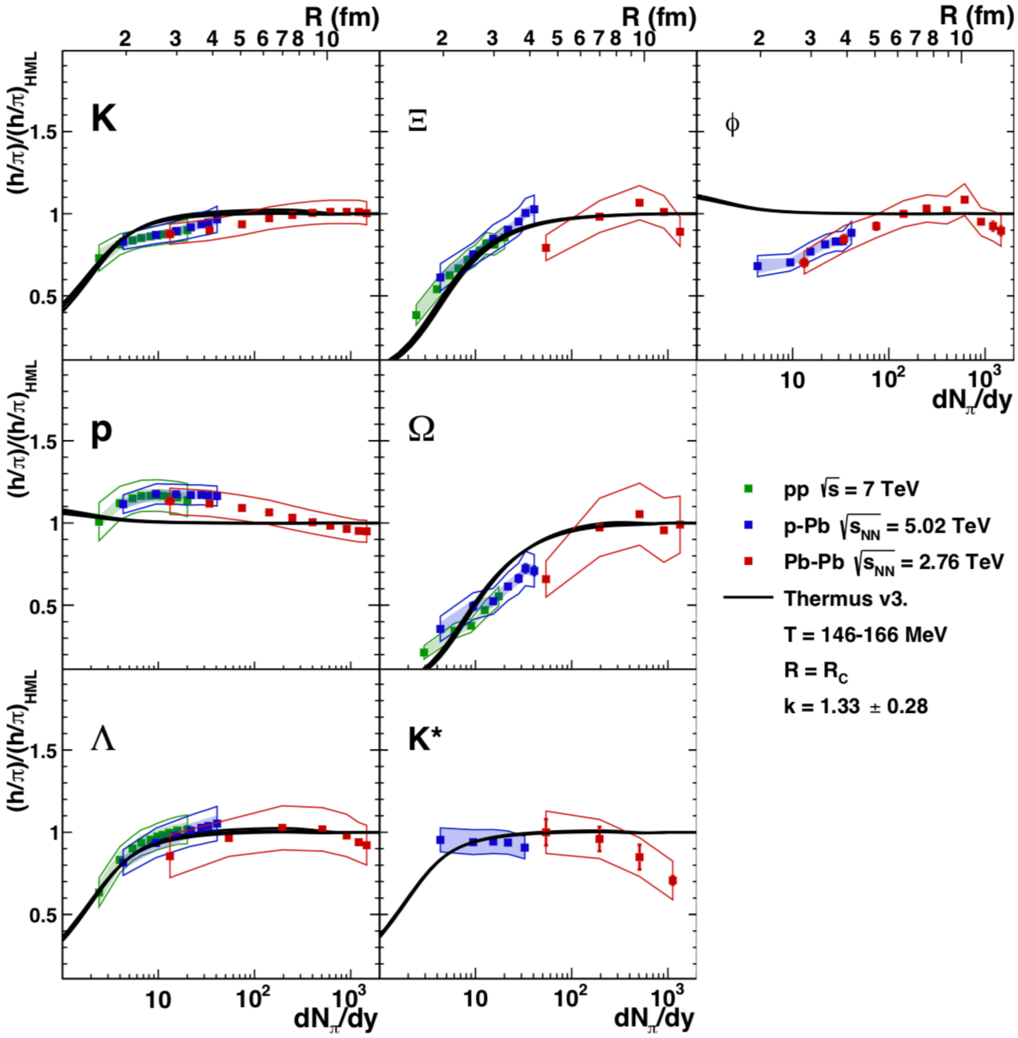

Figure 7: Ratios of several particle species normalized by the high-multiplicity limit. Data points are measured with ALICE, and the canonical suppression model prediction is also shown by black line[11].

2 Experimental setup

2.1 Large Hadron Collider (LHC)

The Large Hadron Collider (LHC) is the largest and highest center of mass energy particle collider in the world, in a tunnel crossing the border of France and Switzerland. It is built by the European Organization for Nuclear Research (CERN) and there are four main experimental facilities, A Toroidal LHC ApparatuS (ATLAS), Compact Muon Solenoid (CMS), A Large Ion Collider Experiment (ALICE), and LHCb. It can collide $\sqrt{s} = 13$ TeV proton beams, and also collide $\sqrt{s_{\mathrm{NN}}} = 5.02$ TeV lead-lead beams. The ALICE is the only experiment specializing in high energy nucleus-nucleus collisions at LHC.

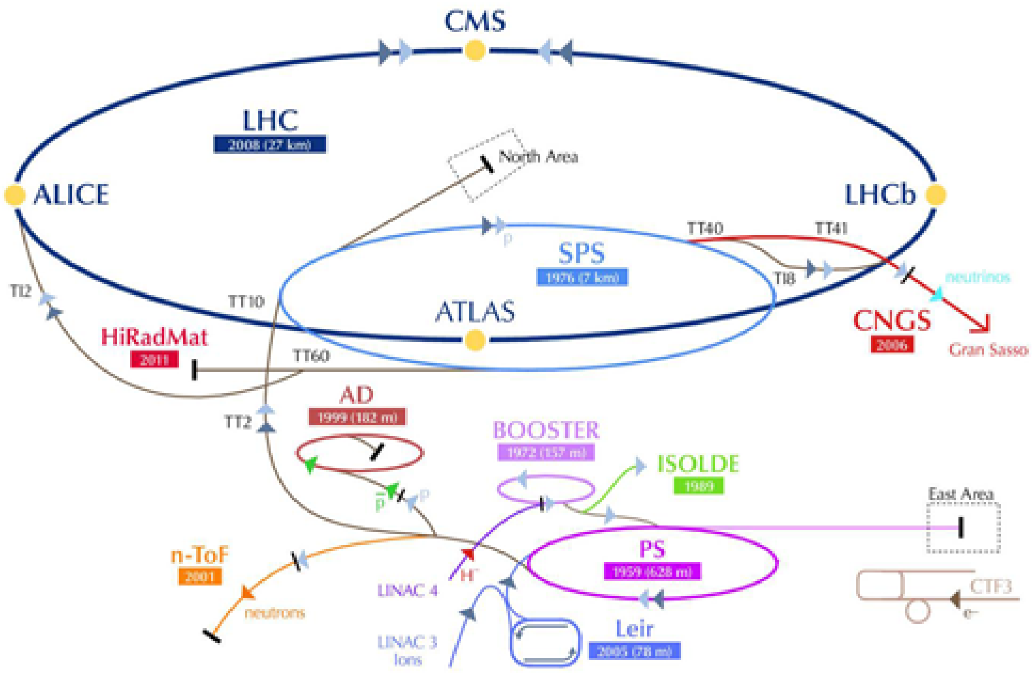

Figure 8: The accelerator complex at CERN[12].

2.2 ALICE detector

ALICE detector is designed to study the strongly interacting matter like QGP, at LHC energies. It has the following three main components. The detector description is from here [13].

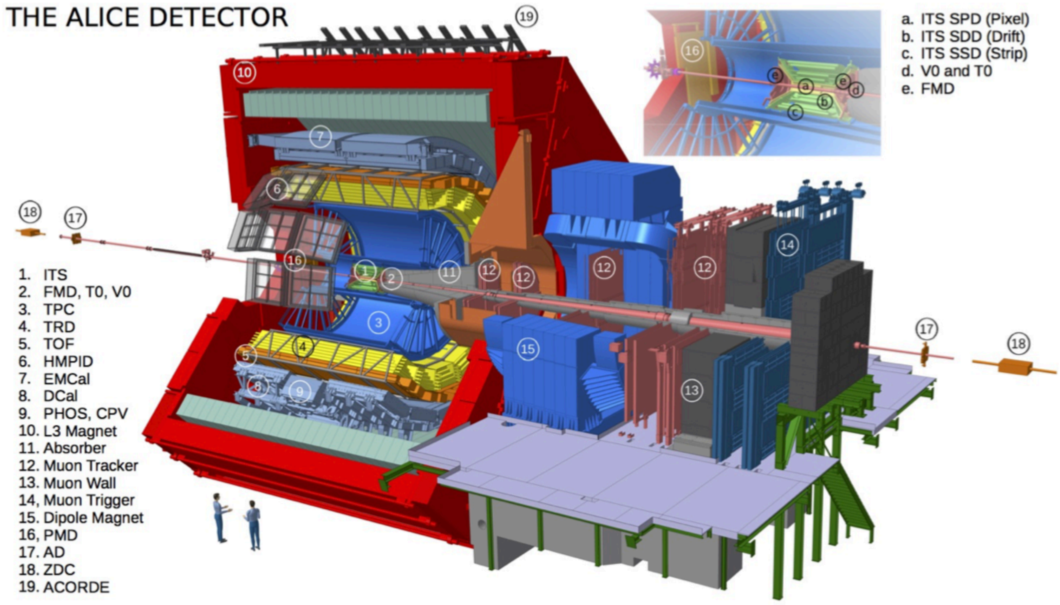

Figure 9: Overview of ALICE detector[15].

(1) Central barrel ($-0.9 < \eta < 0.9$)
(2) Muon Spectrometer ($-4 < \eta < -2.5$)
(3) Global detectors

(1)The central barrel is covered with L3 magnet, which create 0.5 T magnetic field. It provide tracking at mid-rapidity. (2)The muon spectrometer is used for muon measurement at forward rapidity. (3) Global detectors select and classify event.

2.3 Muon Spectrometer

The Muon Spectrometer(Fig.10) is the forward muon detector for the ALICE. It is designed for mainly detect muon decay channel of quarkonia and identify and reconstruct muons. It can measure transverse momentum and charge of passing particles by bending their tracks with the magnetic field and simultaneously identify muons. The main components are the front absorber, the tracking system, the dipole magnet, the muon filter, the trigger system and η coverage is $-4 < \eta < -2.5$.

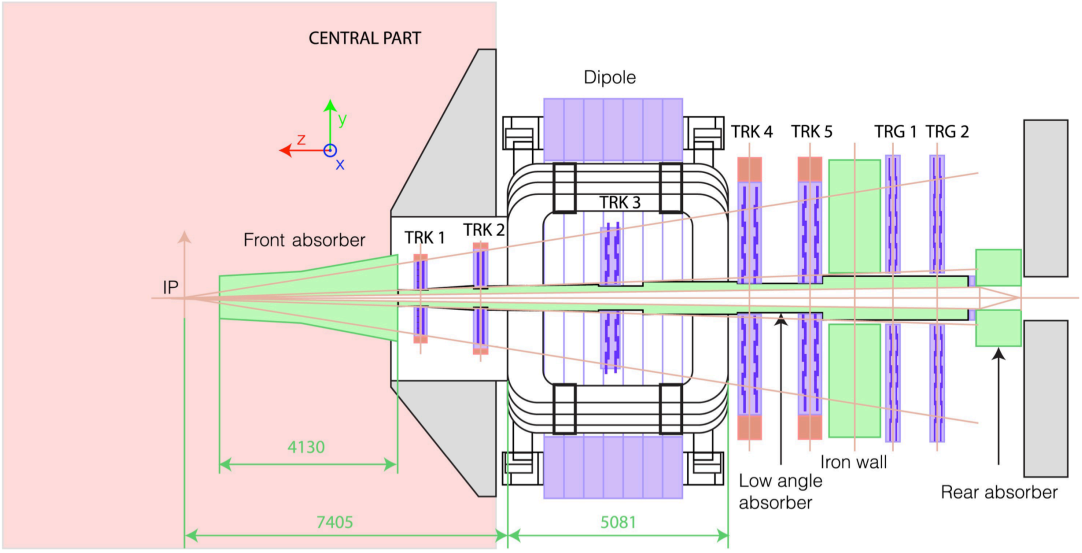

Figure 10: Schematic view of the muon spectrometer[16].

2.3.1 Front absorber

The main purpose of the front absorber is to reduce background muons that comes from pions and kaons. It has 4.13 m of length ($\sim 10\lambda_{int}$) and -90 cm from nominal interaction point. Carbon and concrete, small Z materials, are used in the closest part of it to reduce multiple scattering and lead and tungsten, big Z materials, are used in the back part to absorb the secondary particles from the front absorber.

2.3.2 Tracking system

The tracking system is tracking detectors for muons. It consists of five stations and each station has two Cathode Pad Chambers(CPC). The volume sandwiched between cathodes is filled with the mixed gas of argon and CO_2(80%, 20%). They are ionized by crossing charged particles and create electrons. Anode wires with +1650V are placed between cathodes and electrons are driven by its electric field. A position resolution of this system is $\sim$40 μm.

2.3.3 Dipole magnet

The dipole magnet is mainly composed of horseshoe-shaped coils. It is placed at 7 m from nominal interaction point, and one of the tracking system stations is in it. It can provide $\sim$ 0.7 T magnetic field.

2.3.4 Muon filter

The muon filter is an 1.2 m($\sim 7.2\lambda_{int}$) iron wall. It is placed between the tracking system and trigger system. Its purpose is to reduce background hadrons reaching trigger system.

2.3.5 Trigger System

The trigger system consists of two stations of Resistive Plate Chamber (RPC). Each station has two planes of RPC. The RPC has two bakelite electrode plates, sandwiching mixed gas. Graphite Sheets are put on both outer side of plates for high voltage and readout. This chamber achieves about 2 ns signal rise time and time resolution. This allows short dead time and a reduction of the background.

2.4 Inner Tracking System(ITS)

The ITS(Fig.11) is the innermost detector of ALICE which covers $-0.9 < \eta < 0.9$. The innermost part is called Silicon Pixel Detector(SPD), the middle one is Silicon Drift Detector(SDD), outermost one is Silicon Strip Detector(SSD). Each part has two cylindrical layers. ITS is used for the primary vertex determination, particle identification, and multiplicity determination.

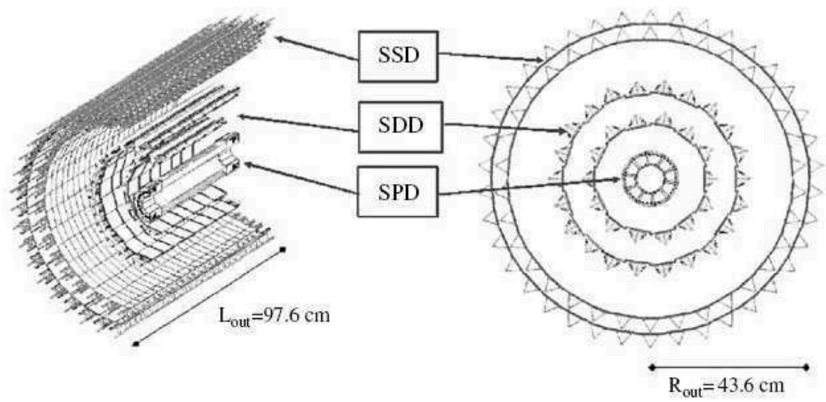

Figure 11: ITS layout[13].

2.5 V0 detectors

The V0 detectors are composed of two arrays of plastic scintillators. Arrays are called V0A and V0C, which cover $2.8 < \eta < 5.1$ and $-3.7 < \eta < -1.7$. They are placed on z = 329 cm(V0A) and z = -88 cm (V0C). They can count signals from collisions, which is important for centrality determination, and their signals are used for triggering(Minimum bias trigger and centrality trigger). Furthermore, they are also used to distinguish beam-beam interactions.

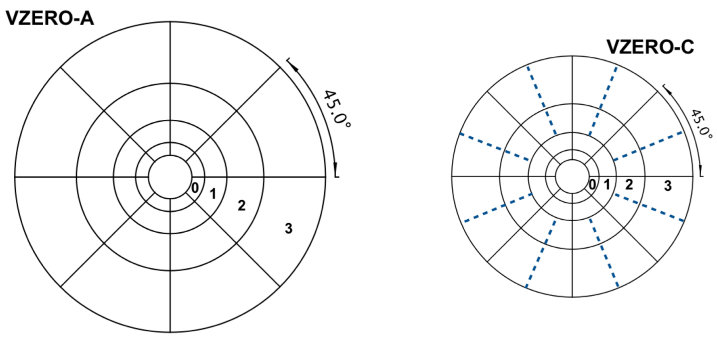

Figure 12: Segmentiation of V0 detectors[14].

3 Analysis

3.1 Data set

In this study, the data sample of p-p run at $\sqrt{s}$ = 13TeV collected with ALICE in 2016 is used. Run periods used in this study are LHC16f, LHC16g, LHC16h, LHC16i, LHC16j, LHC16k, LHC16l, LHC16m, LHC16n, and LHC16o.

3.2 Trigger

3.2.1 Minumum bias trigger

The minimum bias trigger used in this study is CINT7. It is defined as the coincidence of at least one hit each in V0A and V0C at one bunch cross in $|z_{vtx}|$ <10cm.

3.2.2 Muon trigger

Data sample are collected with dimuon unlike-sign(like-sign) low-threshold triggers(CMUL7 and CMLL7) and single muon low-threshold trigger(CMSL7). The CMUL7(CMLL7) is the trigger requiring the coincidence of a minimum bias trigger and at least a pair of unlike-sign(like-sign) matched tracks above the certain transverse momentum threshold on the muon trigger system (0MUL and 0MLL). The CMSL7 requires the coincidence of a minimum bias trigger and at least one matched track above the certain transverse momentum threshold on the muon trigger system(0MSL). The configurations and definitions of muon triggers used in this study are summarized in the following table.

configuration	definition
dimuon trigger	CMUL7 = CINT7 & 0MUL CMLL7 = CINT7 & 0MLL
single muon trigger	CMSL7 = CINT7 & 0MSL

Table 1: Configurations and definitions of muon triggers

Note that CMLL7 are downscaled to 2.4% $\sim$ 50% on a run-b-run basis since they are not signals of the main purpose of the Muon Spectrometer. The data sample in this study is corrected with downscale factor run-by-run.

3.3 Track selection

Track reconstruction and muon identification are performed by the Muon Spectrometer, requiring to match a track on tracking system with a hit on trigger system. χ^2/ndf < 5 is also required for matched tracks. Consequently, muons with $p_{T,\mu} \gtrsim 0.5$ GeV/c are selected, and affect dimuon statistics with transverse momentum $p_{T,\mu\mu} \lesssim 1$GeV/c and invariant mass $M_{\mu\mu} \lesssim 1$ GeV. Therefore, muons with $p_{T,\mu} \lesssim 0.25$ GeV/c are excluded in this study. Muon pseudo-rapidity cut $-4 < \eta_\mu < -2.5$ and passing position cut of the front absorber endcap radius $17.6 < R_{abs} < 89.5cm$ are also applied to reject the muons passing through the acceptance limit. It is also required that hits on different local boards in stations of the trigger system to reject possible trigger bias.

3.4 Multiplicity correction

The multiplicity is obtained from number of SPD tracklets $\mathrm{d}N_{\mathrm{tracklet}}/\mathrm{d}\eta$ measured within $|\eta| < 0.5$ in the MB triggered events , however, SPD acceptance and efficiency along the z vertex position changes event by event because of inactive modules of SPD. In order to estimate z vertex dependent $\mathrm{d}N_{\mathrm{tracklet}}/\mathrm{d}\eta$, the data-driven correction method is employed. In this method, N_{tracklet} is flattened with the correction factor ΔN. It is calculated as

$$\begin{aligned} N_{\mathrm{tracklet}}^{\mathrm{corrected}}(z_{vtx}) &= N_{\mathrm{tracklet}}^{\mathrm{uncorrected}}(z_{vtx}) \cdot \frac{N_{\mathrm{tracklet}}^{ref}}{\langle N_{\mathrm{tracklet}}^{\mathrm{uncorrected}} \rangle (z_{vtx})} \\ &= N_{\mathrm{tracklet}}^{\mathrm{uncorrected}}(z_{vtx}) + \Delta N \end{aligned} \tag{9}$$

where

$$\Delta N = N_{\mathrm{tracklet}}^{\mathrm{uncorrected}}(z_{vtx}) \cdot \frac{N_{\mathrm{tracklet}}^{ref} - \langle N_{\mathrm{tracklet}}^{\mathrm{uncorrected}} \rangle (z_{vtx})}{\langle N_{\mathrm{tracklet}}^{\mathrm{uncorrected}}(z_{vtx}) \rangle (z_{vtx})} \tag{10}$$

where $N_{\mathrm{tracklet}}^{ref}$ is the reference number of tracklets which is mean number of tracklets $\langle N_{\mathrm{tracklet}} \rangle (z_0)$ with the highest efficiency z vertex position z_0 in this study. Poisson distribution with ΔN as a mean value is employed to obtain the integers of ΔN.

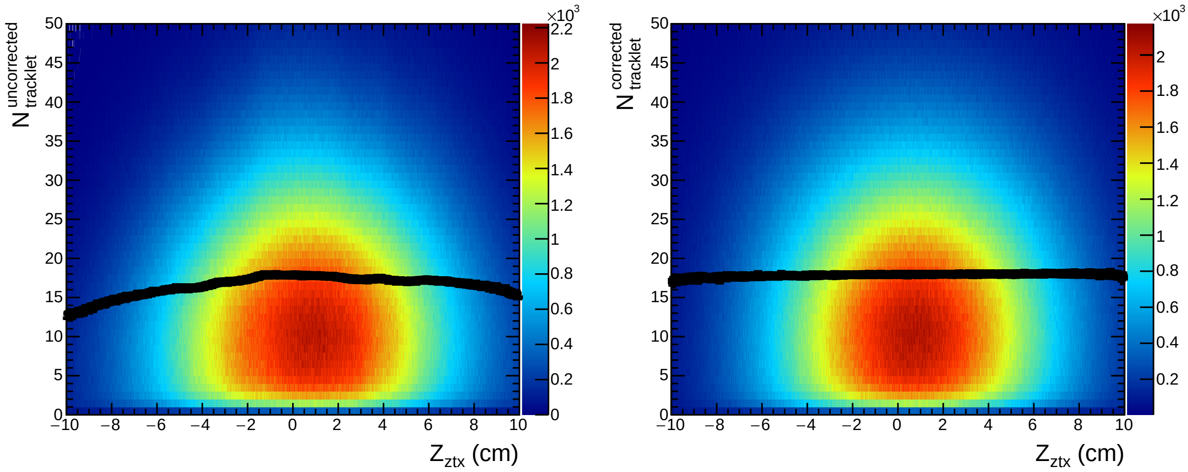

Figure 13: The uncorrected number of tracklets in each z vertex(left panel). The corrected number of tracklets in each z vertex. The mean number of tracklets are also shown with back lines in each panels. The z axis color shows the number of event.

Fig.13 shows the z vertex dependence of $N_{\rm tracklet}$ before and after correction. With this correction, multiplicity distribution can be obtained(Fig.14). It enables to calculate the relative multiplicity $(\mathrm{d}N_{\rm tracklet}^{\rm corrected}/\mathrm{d}\eta)/\langle \mathrm{d}N_{\rm tracklet}^{\rm corrected}/\mathrm{d}\eta\rangle$, where $\langle \mathrm{d}N_{\rm tracklet}^{\rm corrected}/\mathrm{d}\eta\rangle$ is event averaged multiplicity. It is simply calculated as

$$\left(\frac{\mathrm{d}N_{\rm tracklet}^{\rm corrected}/\mathrm{d}\eta)}{\langle \mathrm{d}N_{\rm tracklet}^{\rm corrected}/\mathrm{d}\eta\rangle}\right)_i = \frac{\langle N_{\rm tracklet}^{\rm corrected}\rangle_i}{\langle N_{\rm tracklet}^{\rm corrected}\rangle} \tag{11}$$

where i is each multiplicity range and $\langle N_{\rm tracklet}^{\rm corrected}\rangle$ is averaged number of corrected tracklets.

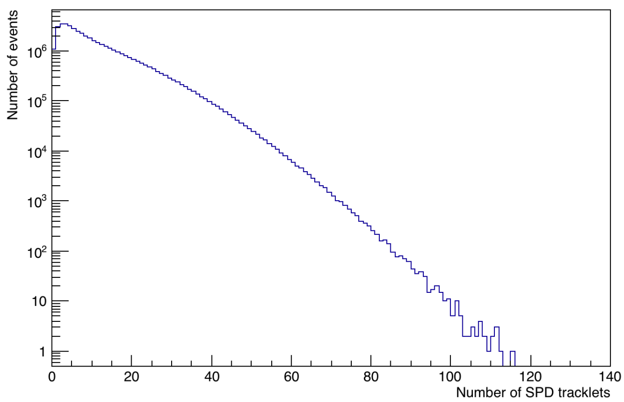

Figure 14: Corrected multiplicity distribution in MB event

3.5 Invariant mass reconstruction

Since mesons decay very soon after their generation, they cannot be detected directly. Therefore, their invariant mass is reconstructed from energy and momentum of their daughter particles from their decay. In this section, the method for invariant mass reconstruction is explained.
The energy of a meson is given by Eq.1,

$$E^2 = M^2 + |\vec{p}|^2 \tag{12}$$

where M^2 and p^2 are invariant mass and momentum of a meson. Then, E and p are expressed as follow,

$$E = E_{\mu^+} + E_{\mu^-} \tag{13}$$

$$\vec{p} = \vec{p}_{\mu^+} + \vec{p}_{\mu^-} \tag{14}$$

where $E_{\mu^\pm}$ and $p_{\mu^\pm}$ are energy and momentum of muons from a meson. With Eq.2 and Eq.3, Eq.1 is expressed as

$$M^2 = E_{\mu^-}^2 + E_{\mu^+}^2 + 2E_{\mu^-}E_{\mu^+} - (|\vec{p_{\mu^-}}|^2 + |\vec{p_{\mu^+}}|^2 + 2\vec{p_{\mu^-}} \cdot \vec{p_{\mu^+}}). \tag{15}$$

Hence, the invariant mass of a meson is given

$$M = \sqrt{E_{\mu^-}^2 + E_{\mu^+}^2 + 2E_{\mu^-}E_{\mu^+} - (|\vec{p_{\mu^-}}|^2 + |\vec{p_{\mu^+}}|^2 + 2\vec{p_{\mu^-}} \cdot \vec{p_{\mu^+}})}. \tag{16}$$

3.6 Signal extraction

Using the method in the previous section, the invariant mass of a meson is calculated. However, muons from mesons cannot be exclusively selected with the detectors. Therefore, invariant mass spectra include all combinations of muons. This invariant mass spectrum consists of uncorrelated dimuon background, correlated dimuon background and light vector meson invariant mass spectrum. In this study, two-step method, uncorrelated dimuon background subtraction and correlated background subtraction are utilized.

3.6.1 Uncorrelated dimuon background

The uncorrelated dimuon background, so-called combinatorial background, comes from the decay of different parents particles. To estimate uncorrelated background, like-sign method is used. In this method, like-sign dimuon invariant mass spectrum is assumed to reproduce uncorrelated invariant mass spectrum. The uncorrelated mass spectrum reproduced with like-sign method N_{CB} is given by

$$N_{CB} = 2R\sqrt{N_{++}^{same}N_{--}^{same}} \tag{17}$$

where N_{++}^{same} and N_{--}^{same} are the like-sign dimuon mass spectra in the same collision event. R factor is the scale factor to correct the different acceptance of $++$, $--$, and $+-$ dimuons and to scale the like-sign dimuon spectra. R factor is given by

$$R = \frac{N_{+-}^{mixed}}{2\sqrt{N_{++}^{mixed} N_{--}^{mixed}}} \tag{18}$$

where N_{++}^{mixed}, N_{--}^{mixed} and N_{+-}^{mixed} are the numbers of mixed event dimuons of each charge combination. Mixed event dimuon is the muon pair from different events, which reproduces uncorrelated dimuon spectrum in all charge combinations. calculating the ratio of unlike-sign mixed dimuon spectrum and like-sign mixed dimuon spectrum, R factor is obtained.

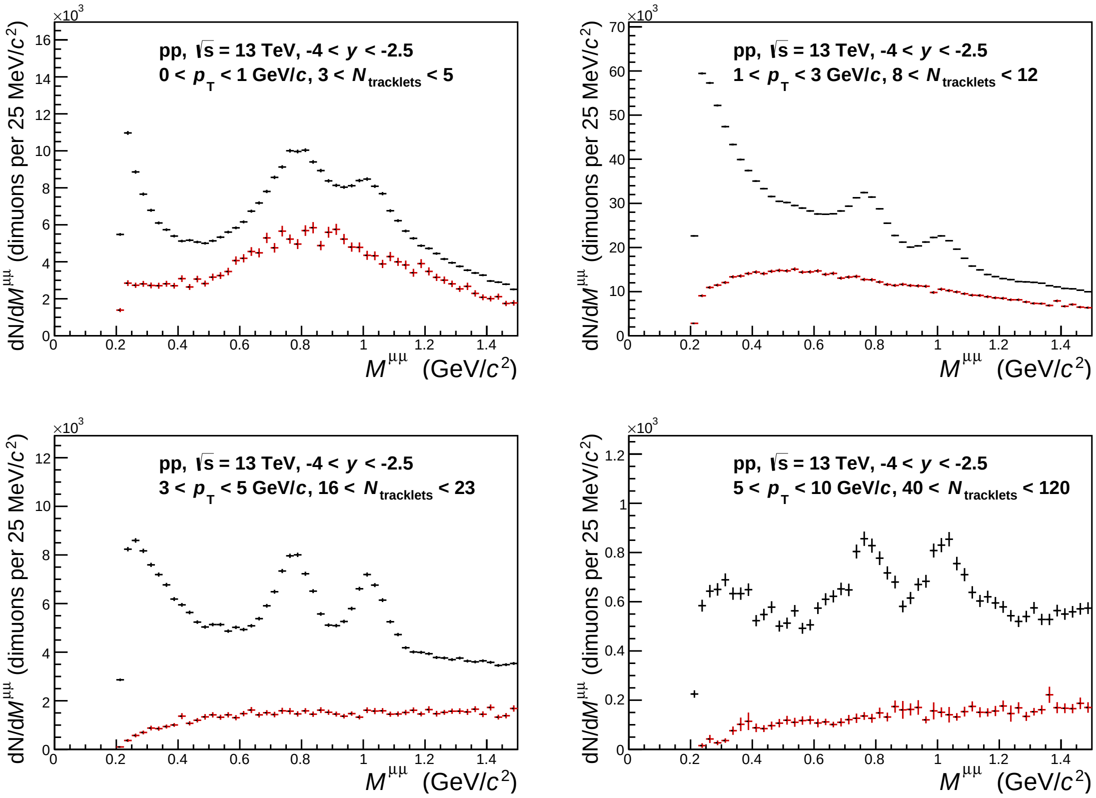

Figure 15: Reconstructed unlike-sign dimuon mass spectrum(black) and combinatorial background(red) in different multiplicity and p_{T} bins.

Fig.15 shows reconstructed unlike-sign dimuon mass spectra and combinatorial background. ϕ and ω meson resonance peaks are visible in these spectra.

3.6.2 Correlated dimuon background

After subtracting the uncorrected dimuon background, the correlated dimuon background is still remaining. Main sources of correlated dimuon background are from two-body decay, Dalitz decay of the light flavored mesons and semi-leptonic decay of D mesons and B mesons. Fitting with some empirical functions(detailed in A.5) is employed to subtract correlated dimuon background. In this fit, the normalization ratio of ω and ρ spectral functions are fixed, requiring $\sigma_\omega = \sigma_\rho$. This is suggested in pp datas and model calculations [17][18]. To fix $\sigma_\omega = \sigma_\rho$, single simulation is operated because mass spectra of these mesons are resulting from convolution of decay width and detector resolution. Therefore, $A \times \epsilon$ of mesons are needed to take account for detector response of resulting invariant mass spectra, where A is the geometrical acceptance and ϵ is the reconstruction efficiency. In this simulation, Pythia8 generator and its parametrization are used in order to generate ω and ρ mesons in pp $\sqrt{s}$ =13 TeV. Then, generated particles are transported and exposed to ALICE detectors, and mass spectra including detector resolution is reconstructed.(Fig.16 and Fig.18) They are fitted with CrystalBall function(See A.0) and counted their yield within $\pm 3\sigma$. From that yield and number of generated mesons toward $-4 < \eta_\mu < -2.5$, $A \times \epsilon$ of mesons are obtained. To obtain p_T spectra of ϕ meson, its simulation is also operated in the same way.

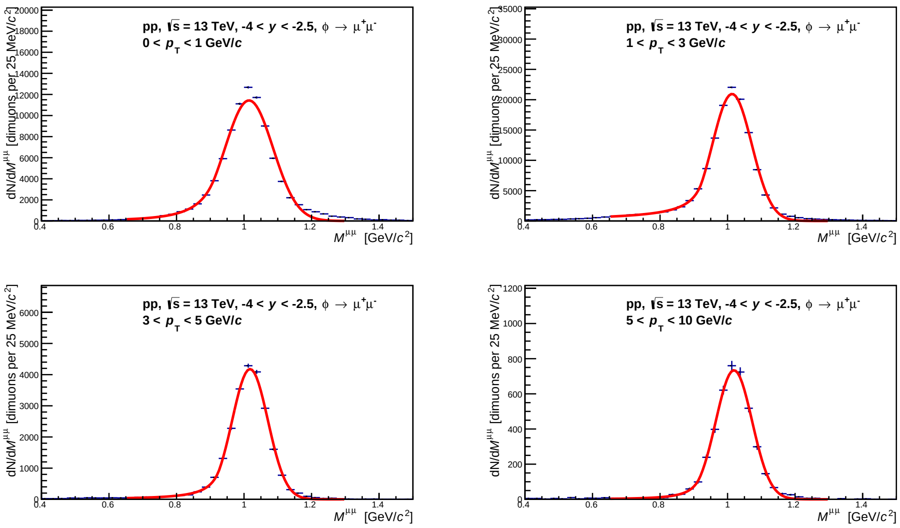

Figure 16: Simulated invariant mass spectra of ϕ meson in each p_{T} bins. Red line is the result of CB function.

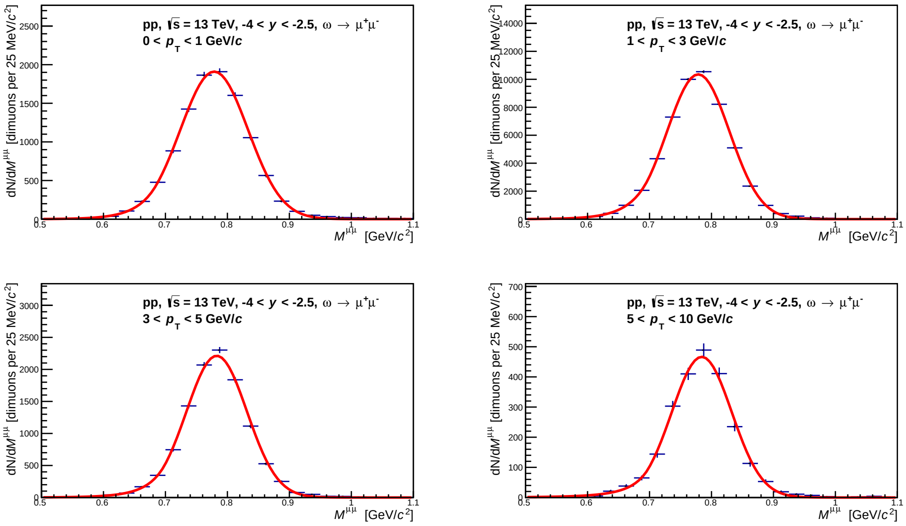

Figure 17: Simulated invariant mass spectra of ω meson in each p_{T} bins. Red line is the result of CB function.

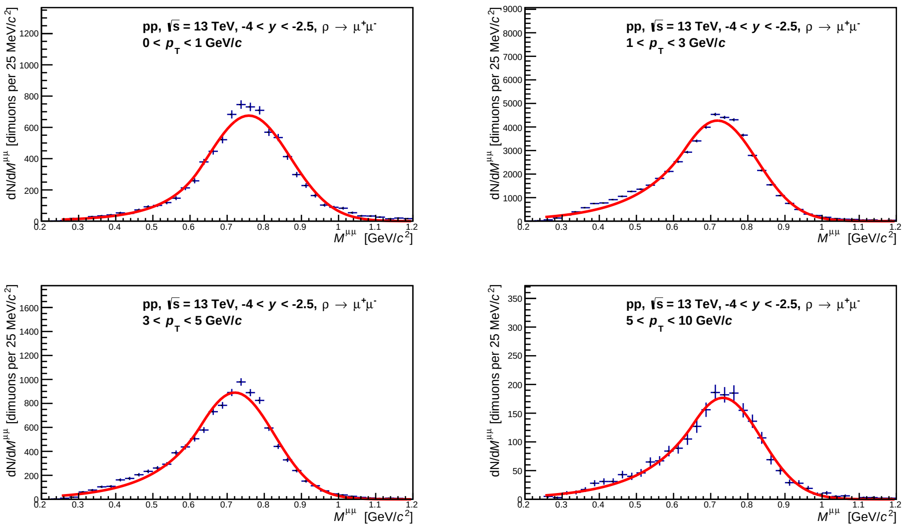

Figure 18: Simulated invariant mass spectra of ρ meson in each p_{T} bins. Red line is the result of CB function.

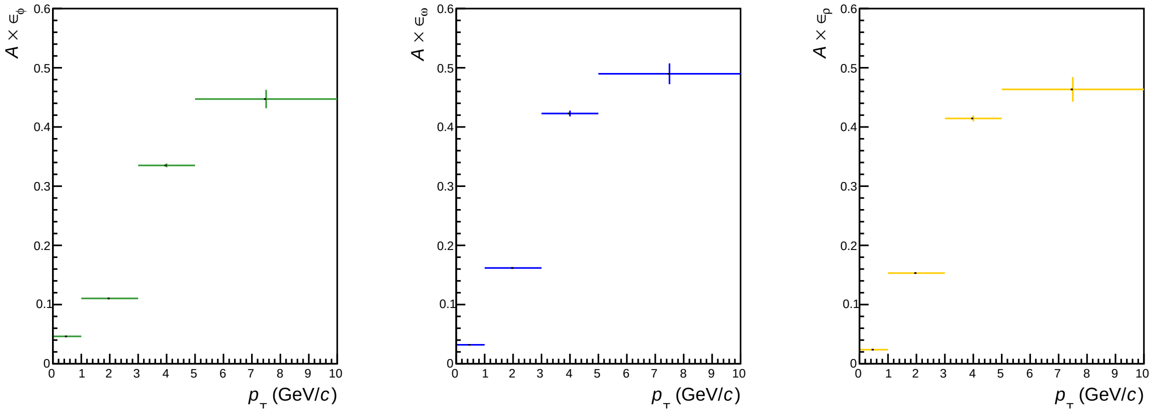

Figure 19: Acceptance $\times$ efficiency for each light vector mesons. Left panel : ϕ meson, mid panel : ω meson, right panel : ρ meson

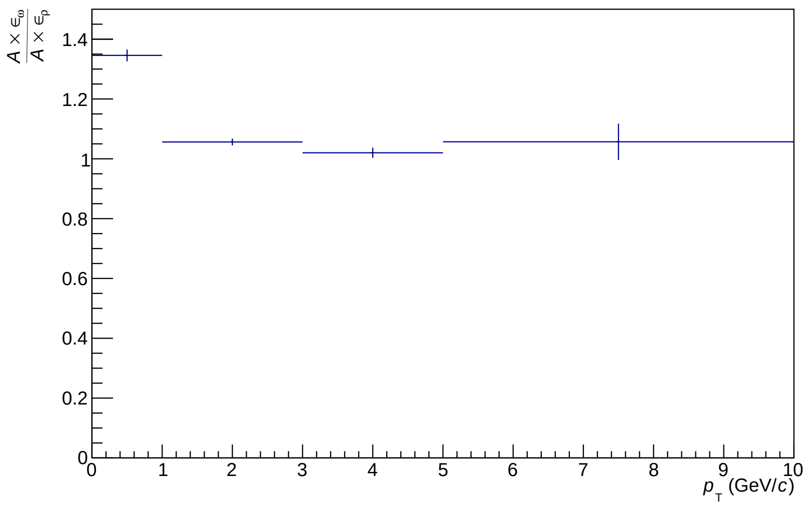

Figure 20: $A \times \epsilon$ ratio of ϕ and ω meson as a function of p_{T}.

The $A \times \epsilon$ ratio is shown in Fig.20. Using this ratio and branching ratios of each mesons, $BR_{\omega\to\mu^+\mu^-} = (9.1 \pm 3.1) \times 10^{-5}$ and $BR_{\rho\to\mu^+\mu^-} = (4.55 \pm 0.28) \times 10^{-5}$, $\sigma_\omega = \sigma_\rho$ can be fixed.

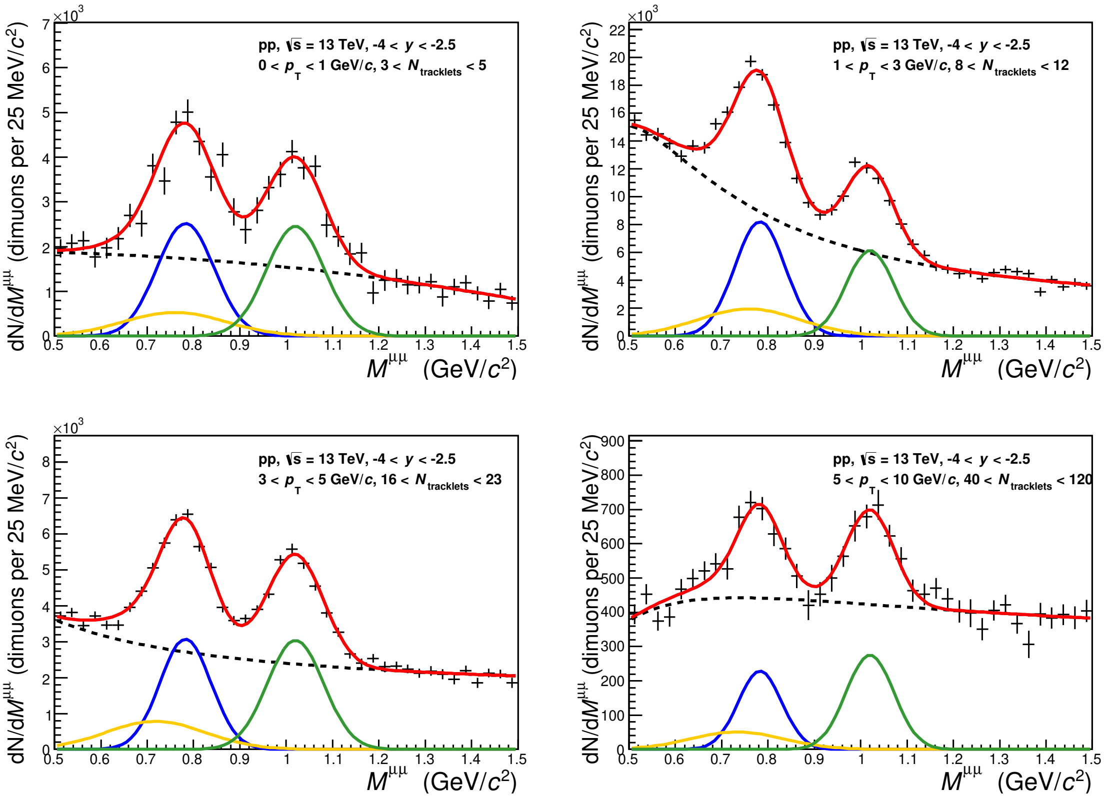

Figure 21: Fitting results of invariant mass spectra in each p_T and multiplicity bins. Red line: inclusive spectra, green line : ϕ,blue line : ω, yellow line : ρ.

Fig.21 shows the fitting results with three gaussians and a variable-width gaussian. From this fitting, ω and ϕ peaks are separated.

3.7 Light vector meson yield

The yields Y^i of light vector mesons in each multiplicity i are calculated as

$$Y^i = \frac{\mathrm{d}N}{\mathrm{d}y\mathrm{d}p_{\mathrm{T}}} = \frac{N^i_{raw}}{BR_{\mu\mu} \cdot A \times \epsilon \cdot N^i_{\mathrm{MB}}} \tag{19}$$

where N^i_{raw} is raw number of light vector mesons decayed into dimuon, N^i_{MB} is number of MB event in each multiplicity. N^i_{MB} is obtained from

$$N^i_{MB} = \sum_{j=\mathrm{run}} F^{i,j}_{\mathrm{norm}} \times N^{i,j}_{\mathrm{MUL}} \tag{20}$$

where $F^{i,j}_{\mathrm{norm}}$ is the rejection factor of dimuon trigger in each run j to convert the number of analyzed unlike-sign dimuon events to that of MB events, and $N^{i,j}_{\mathrm{MUL}}$ is the number of analyzed dimuon triggers. In this study, the following method is used to evaluate the rejection factor as

$$F^{i,j}_{\mathrm{norm}} = \frac{\mathrm{MB}^{i,j}}{(\mathrm{MB\&0MSL})^{i,j}} \times \frac{\mathrm{MSL}^{i,j}}{(\mathrm{MSL\&0MUL})^{i,j}} \tag{21}$$

where MB, MSL, 0MSL, and 0MUL are the number of events fulfilling each trigger. F^{i}_{norm} and equivalent multiplicity ranges are summarized in following table.

$N^{corrected}_{tracklet}$	$\frac{\mathrm{d}N^{corrected}_{tracklet}/d\eta}{\langle \mathrm{d}N^{corrected}_{tracklet}/d\eta \rangle}$	Rejection factor F^{i}_{norm}
$1 < N_{tracklet} < 3$	0.21	11987
$3 < N_{tracklet} < 5$	0.39	8059.6
$5 < N_{tracklet} < 8$	0.59	4924.3
$8 < N_{tracklet} < 12$	0.89	3054.1
$12 < N_{tracklet} < 16$	1.2	2296.0
$16 < N_{tracklet} < 23$	1.7	1415.0
$23 < N_{tracklet} < 40$	2.6	932.42
$40 < N_{tracklet} < 120$	4.1	475.74

Table 2: Summary of multiplicity ranges and rejection factors used in this study.

4 Results and discussion

4.1 p_{T} spectrum

Fig.22 shows the p_{T} spectra of ϕ meson in pp collisions at $\sqrt{s} = 13$ TeV in each multiplicity bin.

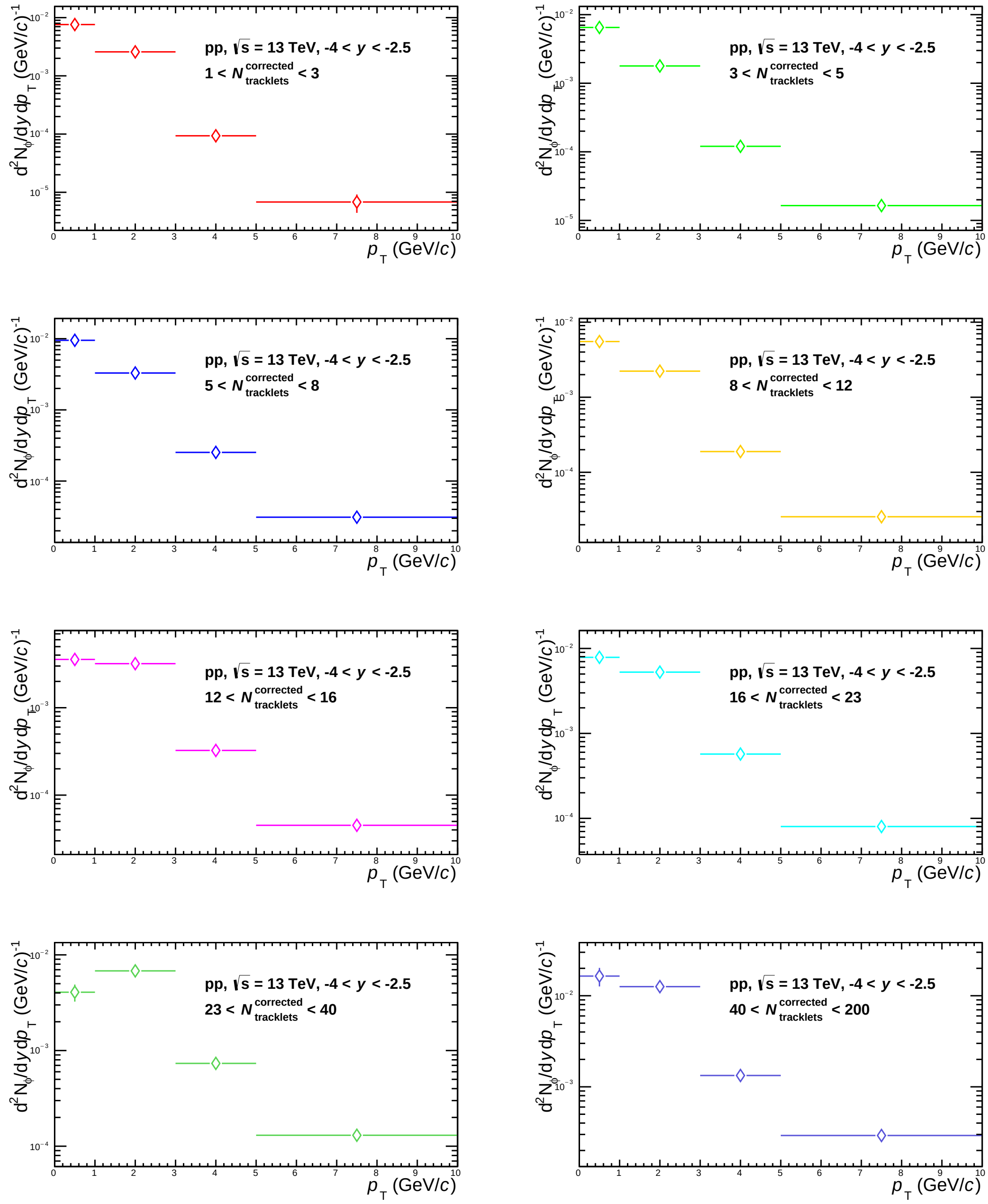

Figure 22: p_{T} spectra of ϕ meson.

Fig.23 shows the p_{T} spectra of ω meson in pp collisions at $\sqrt{s}$ = 13 TeV in each multiplicity bin.

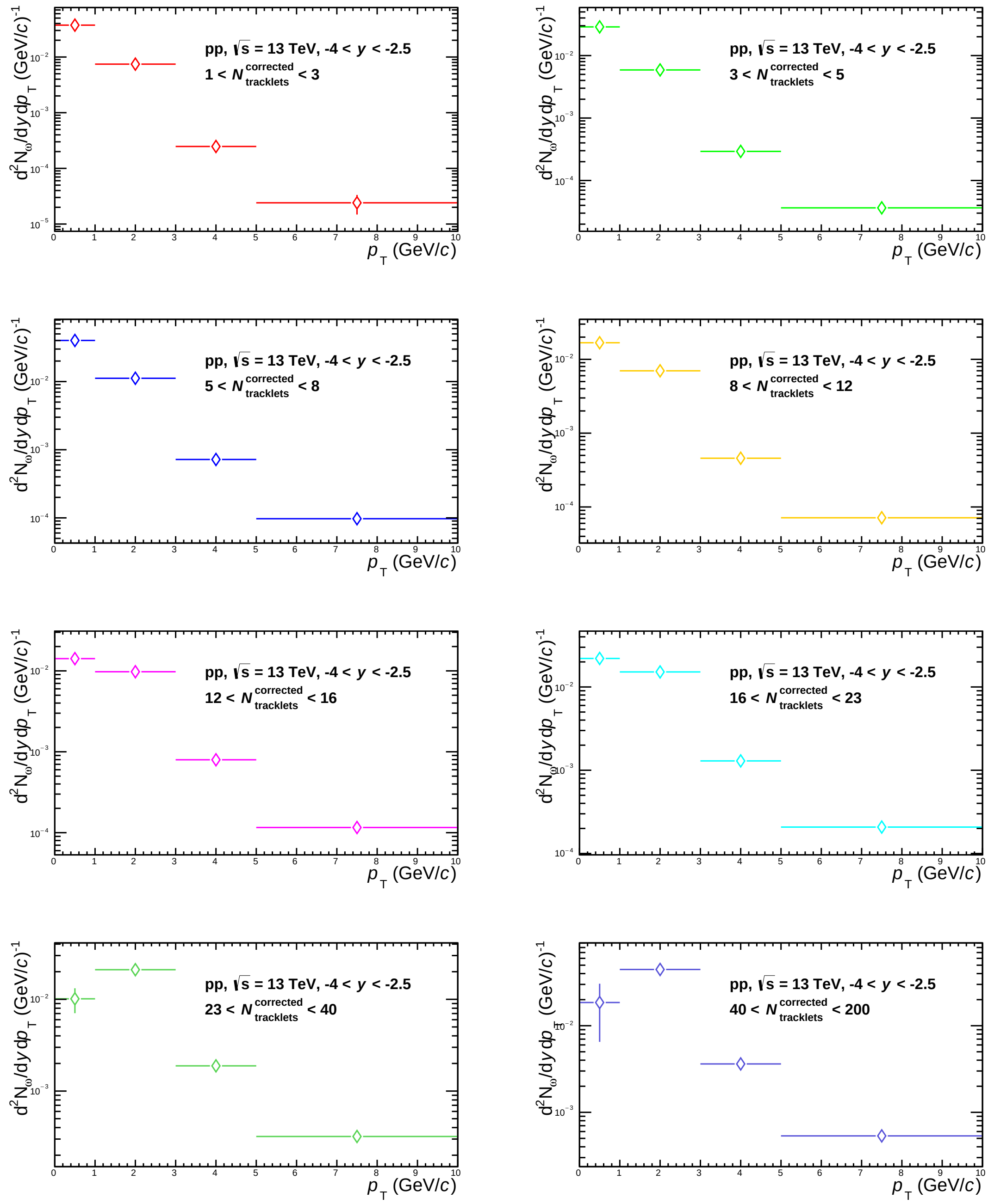

Figure 23: p_{T} spectra of ω meson.

4.2 Self-normalized yield

To estimate the multiplicity dependence of light vector meson, the self-normalized yield is used in this analysis. The self-normalized yield can express the difference of trend between total multiplicity and light vector meson. Moreover, some systematic uncertainty, the branching ratio into dimuon, for instance, is canceled out in the ratios. The self-normalized yield in each multiplicity bin i is calculated by the following formula:

$$\frac{Y^i}{\langle Y^i \rangle} = \frac{N^i_{raw}}{N^{inc}_{raw}} \times \frac{F^{inc}_{\mathrm{norm}}}{F^i_{\mathrm{norm}}} \times \frac{N^{inc}_{\mathrm{MUL}}}{N^i_{\mathrm{MUL}}} \tag{22}$$

where N^{inc}_{raw}, F^{inc}_{norm}, N_{MUL} are multiplicity inclusive ones.

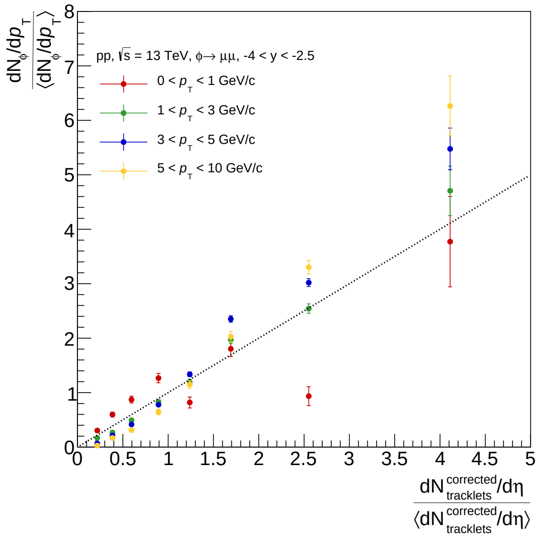

Figure 24: Self-normalized yield of ϕ meson as a function of multiplicity.

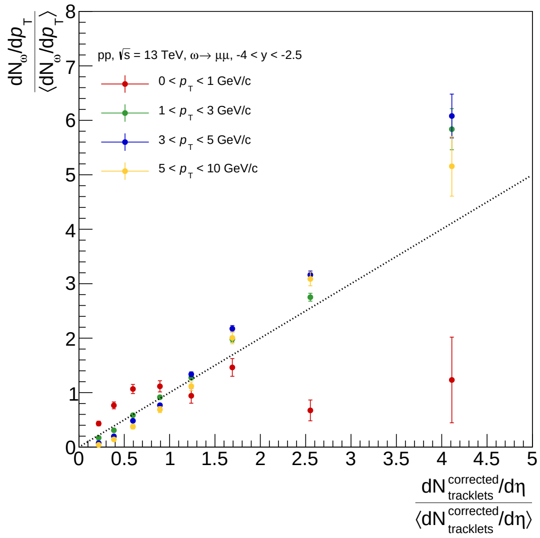

Figure 25: Self-normalized yield of ω meson as a function of multiplicity.

Fig.24 and 25 show the self normalized yields of ϕ and ω meson as a function of multiplicity in p_{T} ranges, $0 < p_{\mathrm{T}} < 1$, $1 < p_{\mathrm{T}} < 3$, $3 < p_{\mathrm{T}} < 5$, $5 < p_{\mathrm{T}} < 10$ GeV/c. Black dashed line is the first diagonal. For ϕ and ω meson, enhancement is observed at $p_{\mathrm{T}} > 1$ GeV/c, in higher multiplicity bins. Similar multiplicity dependence is seen in the both mesons, and this may indicate the same production mechanism.

4.3 Double ratio of ϕ and ω mesons

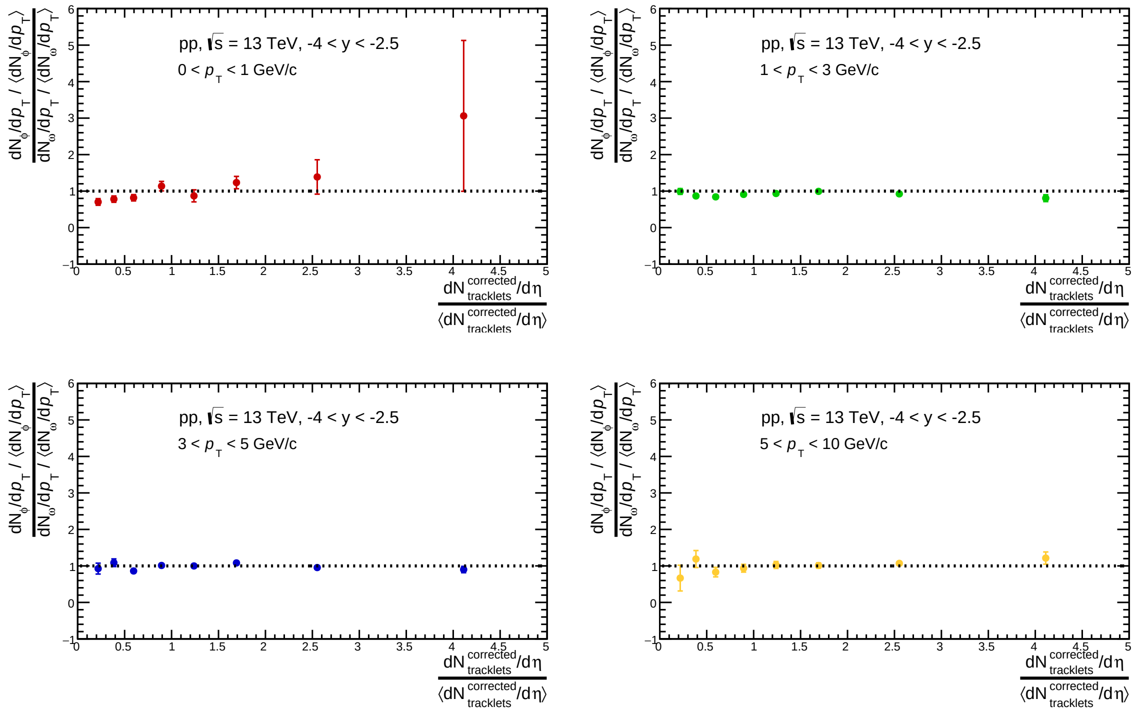

Figure 26: Ratio of self-normalized yield of ϕ and ω meson as a function of multiplicity.

Fig.26 shows the ratio of self-normalized yields of ϕ and ω mesons as a function of multiplicity. This ratio is found to be consistent to a constant. However, the increasing trend in the central value of the ratio seen at p_{T} <1 GeV/c might indicate thermal strangeness production, while no indication of enhancement of ϕ meson relative to ω meson is observed at $p_{\mathrm{T}} > 1$ GeV/c.

5 Conclusion

The self-normalized yields of ϕ and ω mesons are measured via the dimuon decay channel as a function of multiplicity in pp collisions at $\sqrt{s} = 13$ TeV at forward rapidity. At high p_{T} and multiplicity, ϕ and ω mesons are relatively increased. For ω meson, it was relatively reduced at $p_{\mathrm{T}} < 1\mathrm{GeV}/c$, in high multiplicity events. The inclusive behavior of ϕ meson is similar to ω meson.
The ratio of self-normalized yields of ϕ and ω meson is also calculated in the same p_{T} and multiplicity ranges. They were consistent to the unity in all p_{T} and multiplicity. However, this ratio is increasing to factor ≈ 2 at $p_{\mathrm{T}} < 1$ GeV/c. This behavior might originate from thermal $s\bar{s}$ creation, expected to be dominant in low p_{T}. The systematic uncertainty estimation is needed for more detailed study.

6 Acknowledgement

First of all, I would like to thank all staffs in the Quark Physics Laboratory, Assoc. Prof. K Shigaki, Prof. T. Sugitate, Assist. Prof. K. Homma, Assist. Prof. T. Miyoshi. All staffs gave me a lot of important comments for my study. Especially, I cordially appreciate Assoc. Prof. K. Shigaki and Dr.Y. Yamaguchi for their supporting my research, giving me enormous amount of advice, and discussing with me.

I express my gratitude to my seniors, Dr.D. Sekihata, Dr.S. Yano, Dr.K. Nagashima, Y. Ueda, K. Yamakawa for teaching me empirical and scientific things. Their advice greatly helped my research. I also thank Dr. A.Uras for holding PAG meeting for me and giving me advice. Finally, I acknowledge all members of this laboratory. They always kind and helpful for my academic life.

A Appendix

A.1 Gaussian

Gaussian is used for fitting peaks of light vector mesons. This function describes the convolution of Breit-Wigner distribution of resonance and detector resolution.

$$f(x; N, \overline{x}, \sigma) = N \cdot \exp(-\frac{(x-\overline{x})^2}{2\sigma^2}) \tag{23}$$

A.2 CrystalBall function

Crystal Ball(CB) function is composed of a Gaussian and a power-low low-mass tail. Gaussian accounts for the detector resolution and low-mass tail account for energy loss effect. The CB function is defined as follow.

$$f(x; \alpha, n, \overline{x}, \sigma, N) = N \cdot \begin{cases} \exp(-\frac{(x-\overline{x})^2}{2\sigma^2}) & (\frac{x-\overline{x}}{\sigma} > -\alpha) \\ (\frac{n}{\alpha})^n \times \exp(-\frac{\alpha^2}{2}) \times (\frac{n}{\alpha} - \alpha - \frac{x-\overline{x}}{\sigma})^{-n} & (\frac{x-\overline{x}}{\sigma} \leq -\alpha) \end{cases} \tag{24}$$

A.3 Variable-Width Gaussian

Variable-Width Gaussian(VWG) is one of empirical function commonly used for quarkonium study. It is characteristics that the width changes.

$$f(x; N, \overline{x}, A, B) = N \cdot \exp(-\frac{(x-\overline{x})^2}{2\sigma_{VWG}^2}) \tag{25}$$

where

$$\sigma_{VWG} = A + B \cdot \frac{(x-\overline{x})}{\overline{x}}. \tag{26}$$

A.4 Combinatorial background subtraction

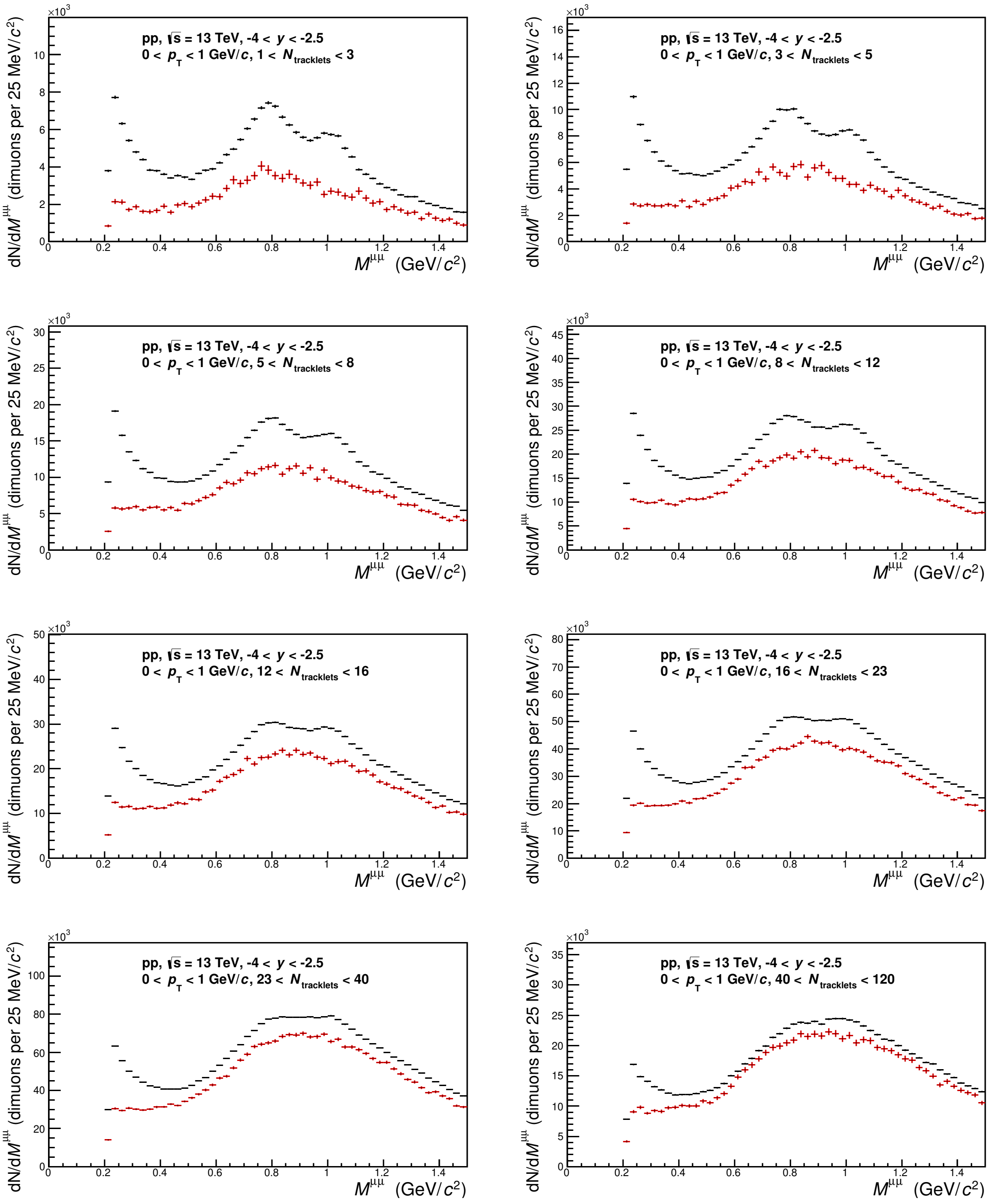

Figure 27: Unlike-sign dimuon mass spectrum(black) and combinatorial background(red) in each multiplicity bin, $0 < p_{\mathrm{T}} < 1$ GeV/c.

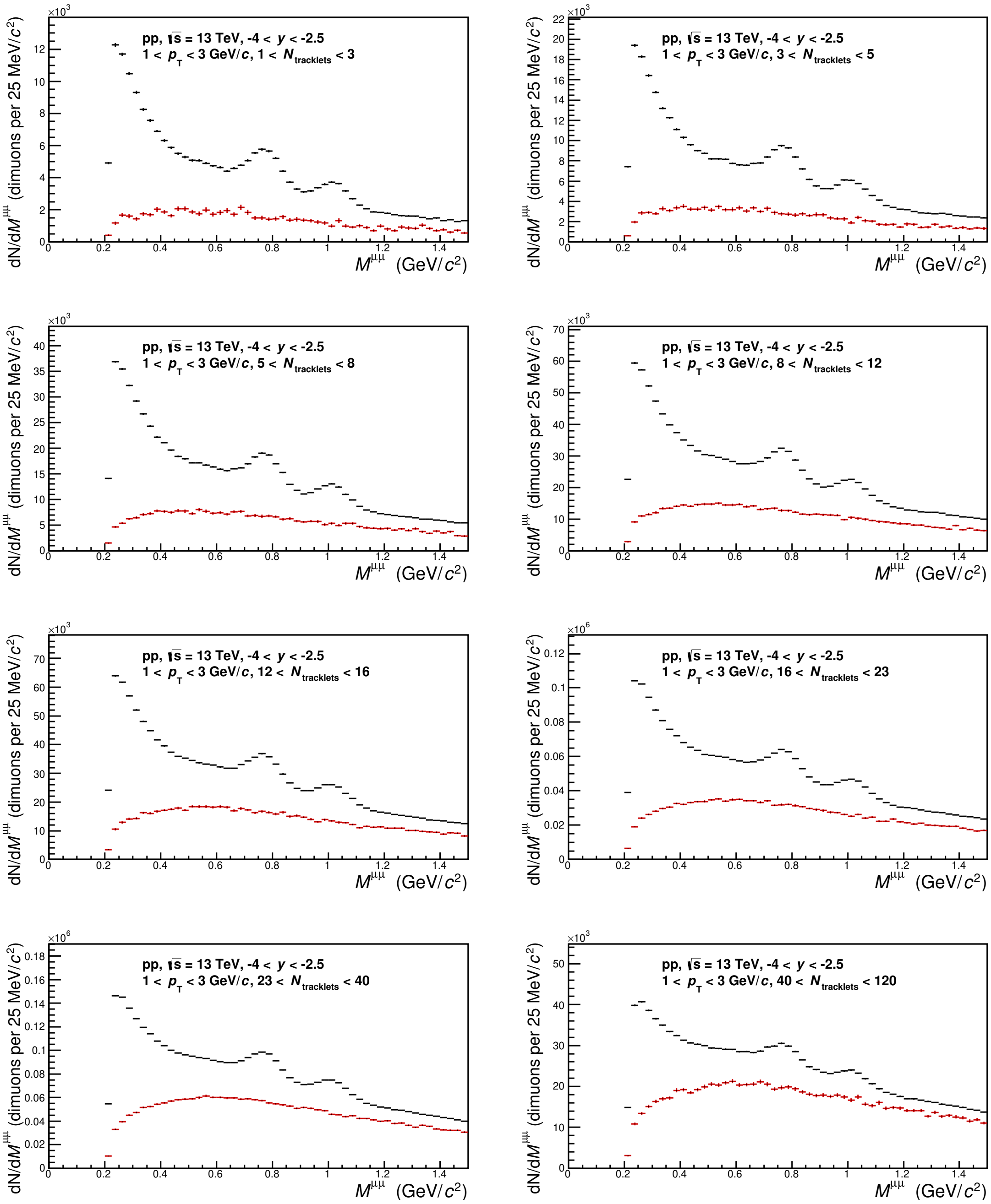

Figure 28: Unlike-sign dimuon mass spectrum(black) and combinatorial background(red) in each multiplicity bin, $1 < p_{\mathrm{T}} < 3$ GeV/c.

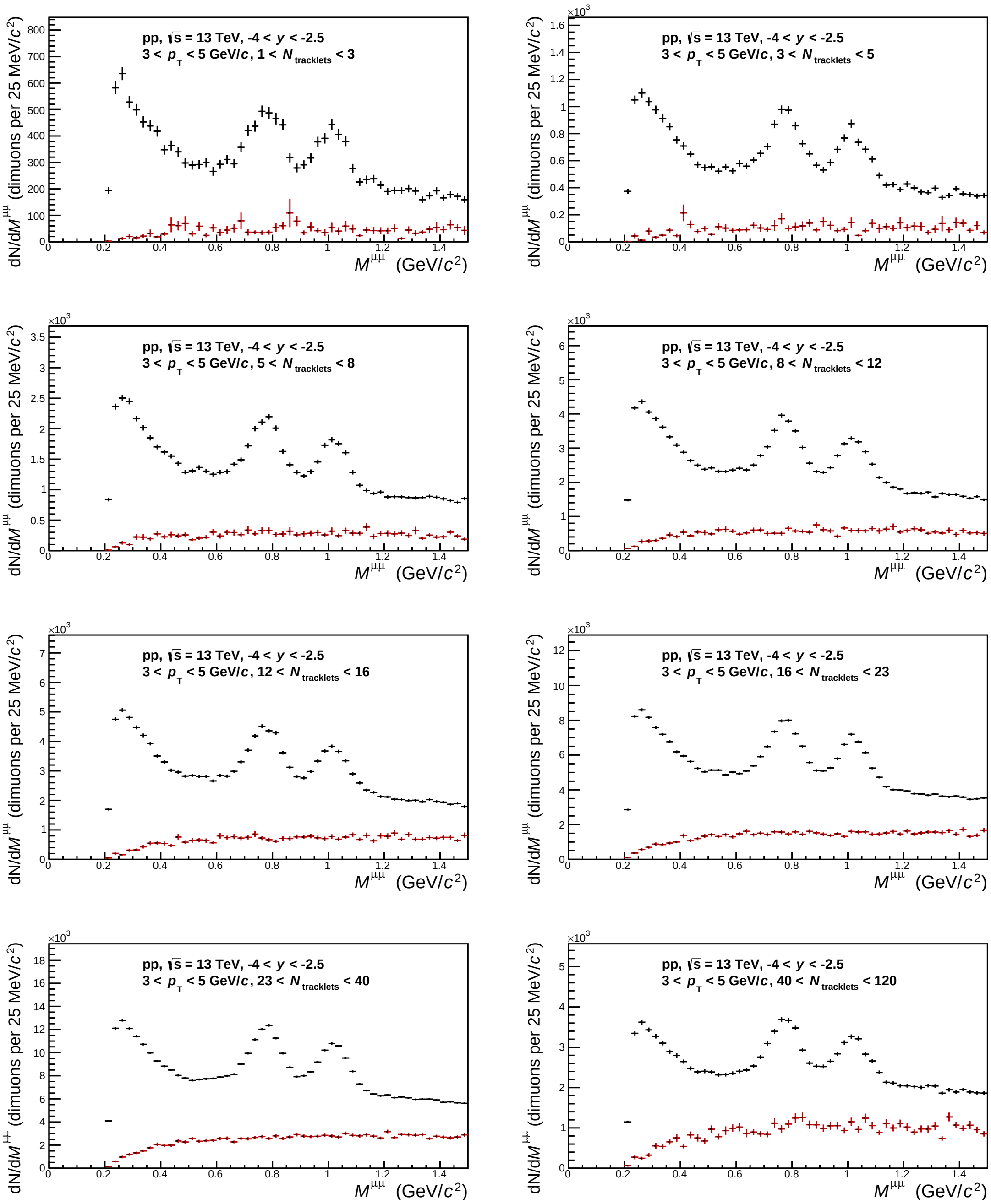

Figure 29: Unlike-sign dimuon mass spectrum(black) and combinatorial background(red) in each multiplicity bin, $3 < p_{\mathrm{T}} < 5$ GeV/c.

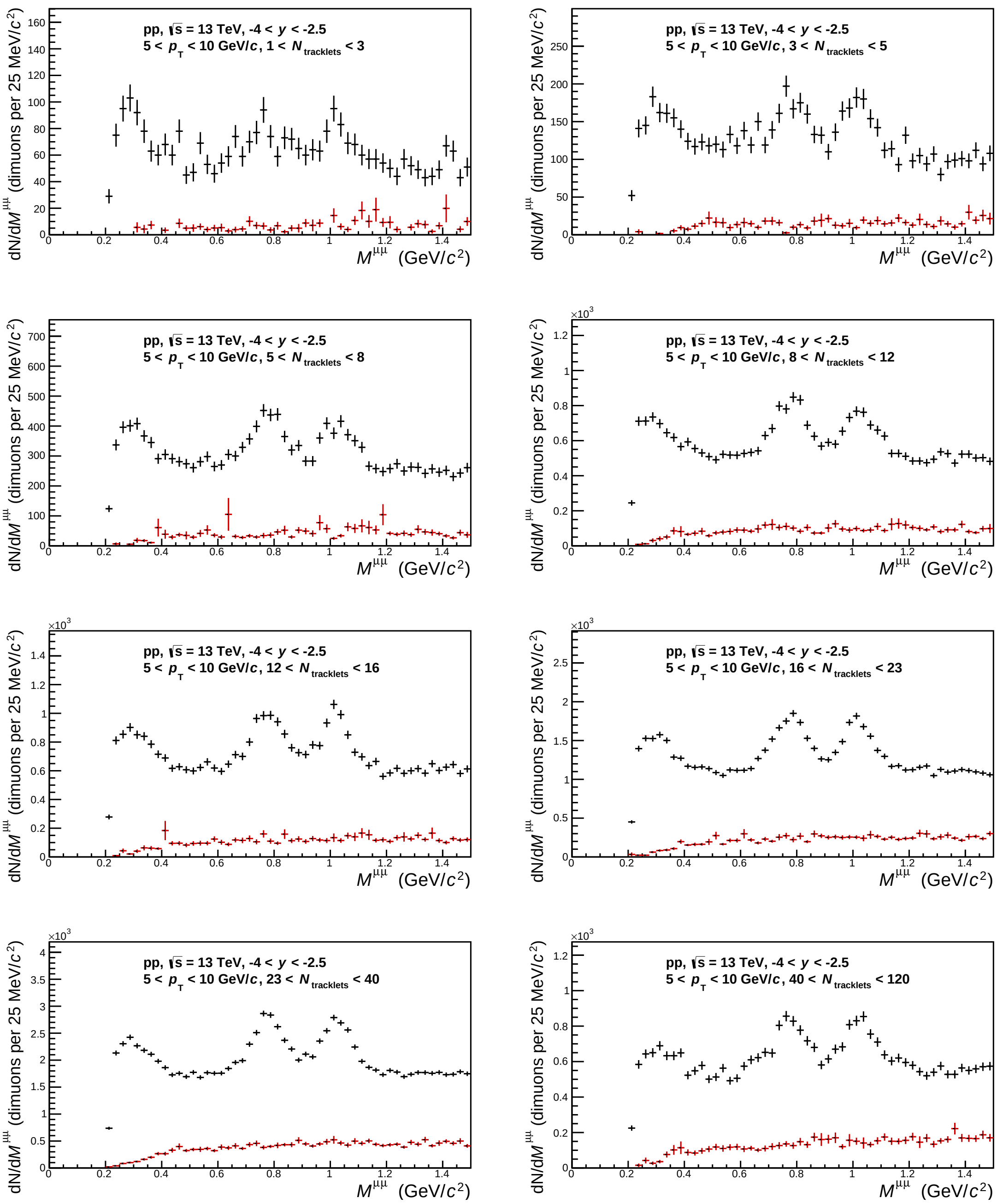

Figure 30: Unlike-sign dimuon mass spectrum(black) and combinatorial background(red) in each multiplicity bin, $5 < p_{\mathrm{T}} < 10$ GeV/c.

A.5 Correlated background subtraction

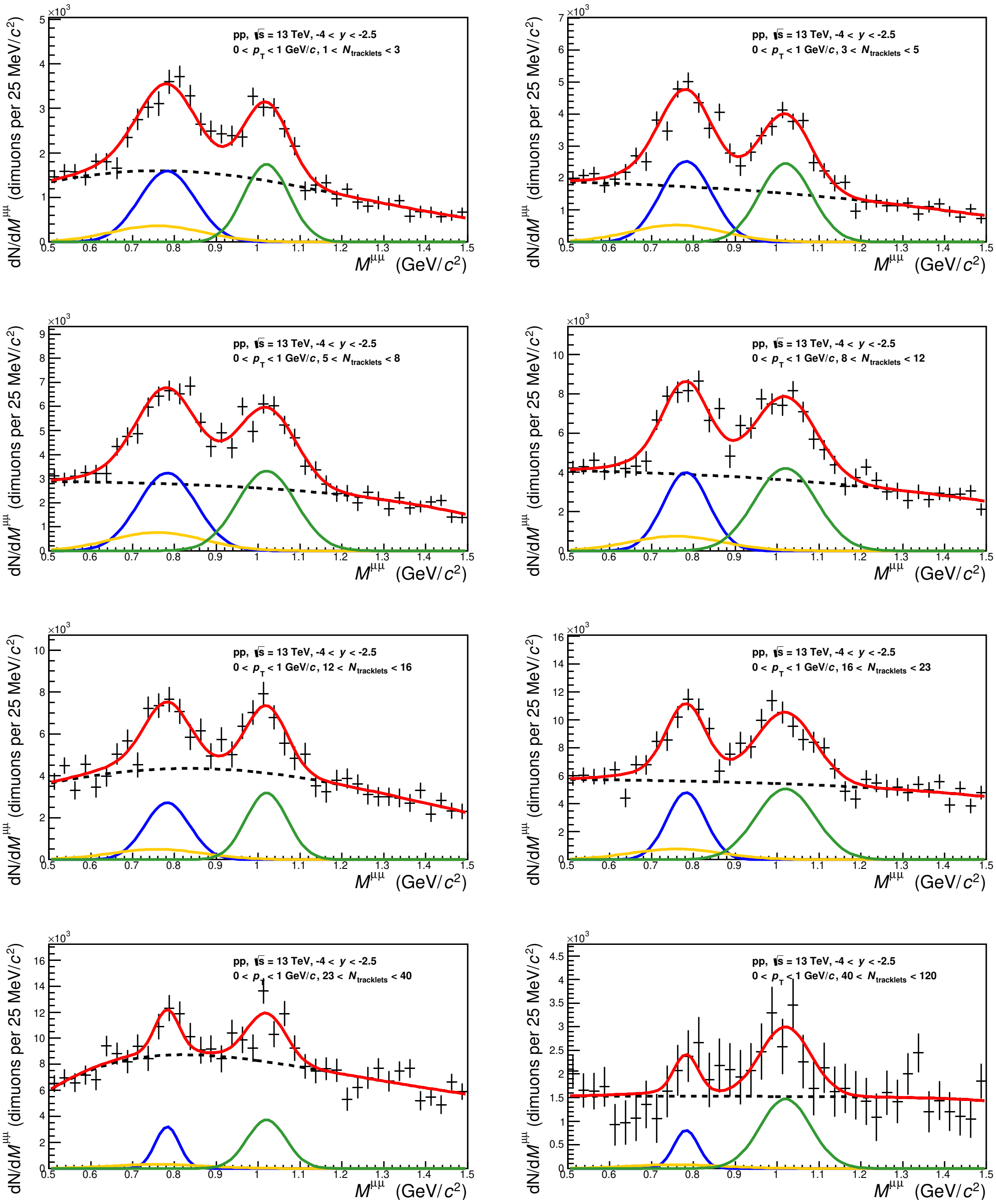

Figure 31: Unlike-sign dimuon mass spectrum subtracted uncorrelated background(histogram), inclusive function(red), ϕ meson gaussian(green), ω meson gaussian(blue), ρ meson gaussian(yellow), and VWG function in each multiplicity bin, $0 < p_{\rm T} < 1$ GeV/c.

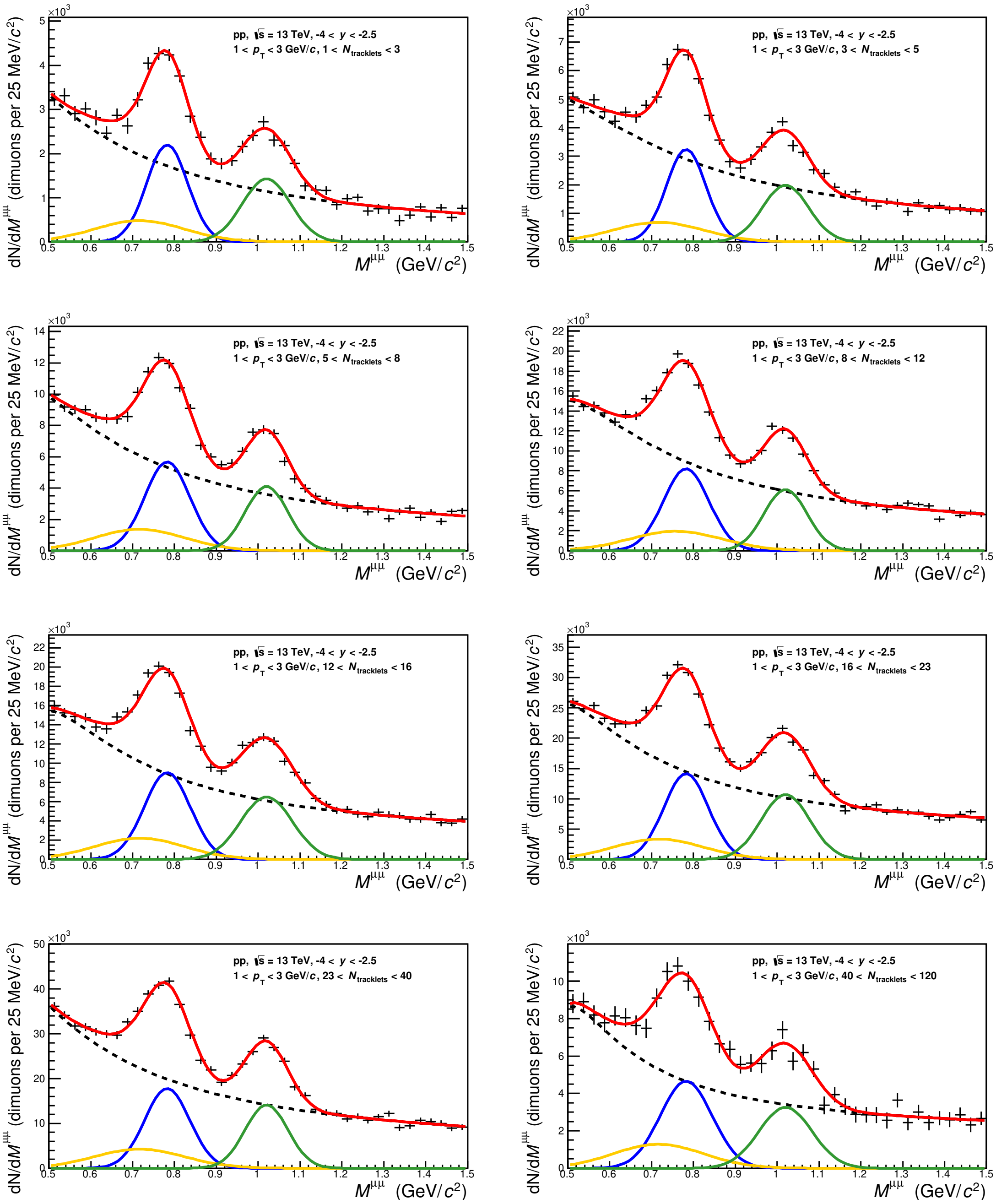

Figure 32: Unlike-sign dimuon mass spectrum subtracted uncorrelated background(histogram), inclusive function(red), ϕ meson gaussian(green), ω meson gaussian(blue), ρ meson gaussian(yellow), and VWG function in each multiplicity bin, $1 < p_{\mathrm{T}} < 3$ GeV/c.

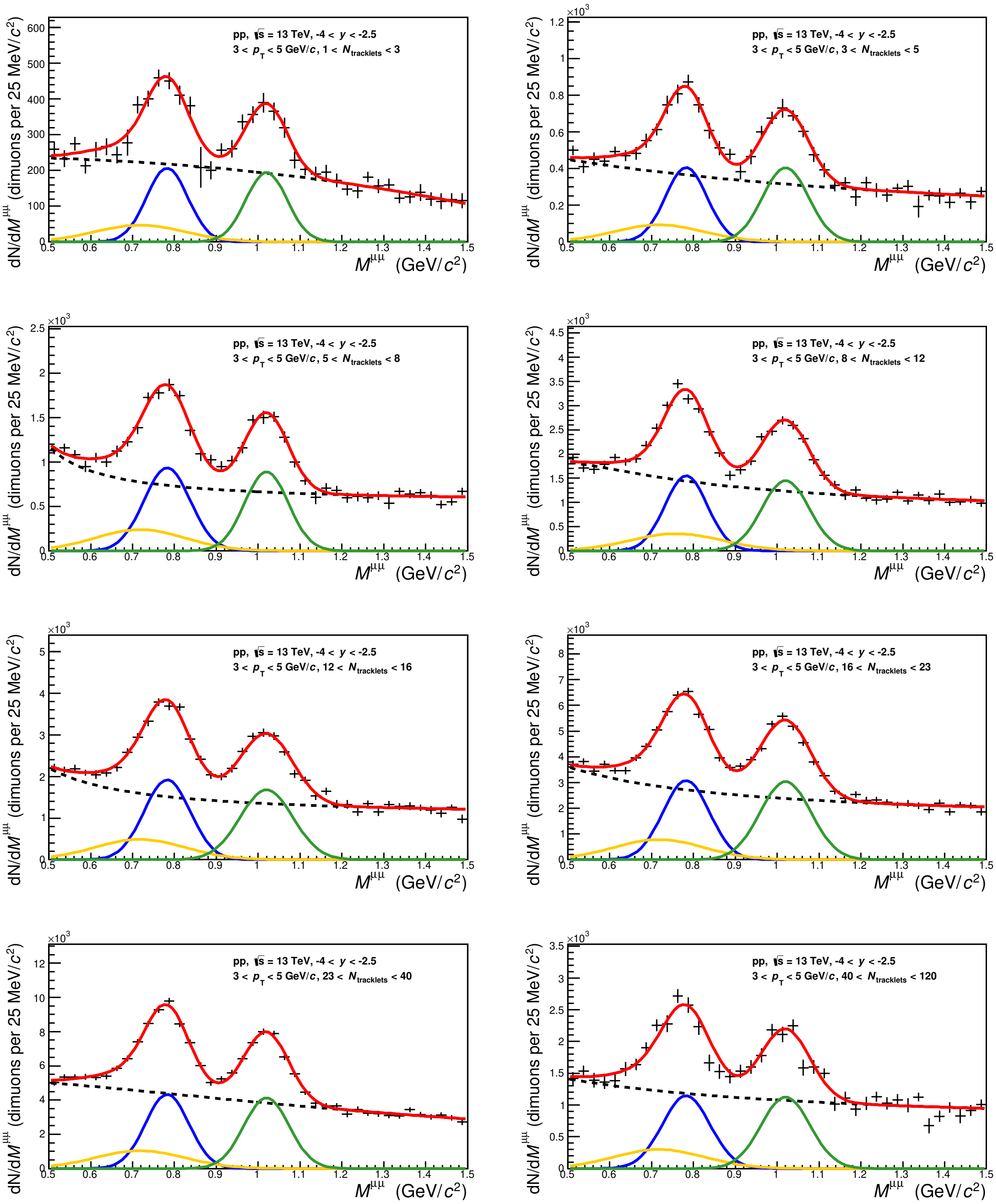

Figure 33: Unlike-sign dimuon mass spectrum subtracted uncorrelated background(histogram), inclusive function(red), ϕ meson gaussian(green), ω meson gaussian(blue), ρ meson gaussian(yellow), and VWG function in each multiplicity bin, $3 < p_{\mathrm{T}} < 5$ GeV/c.

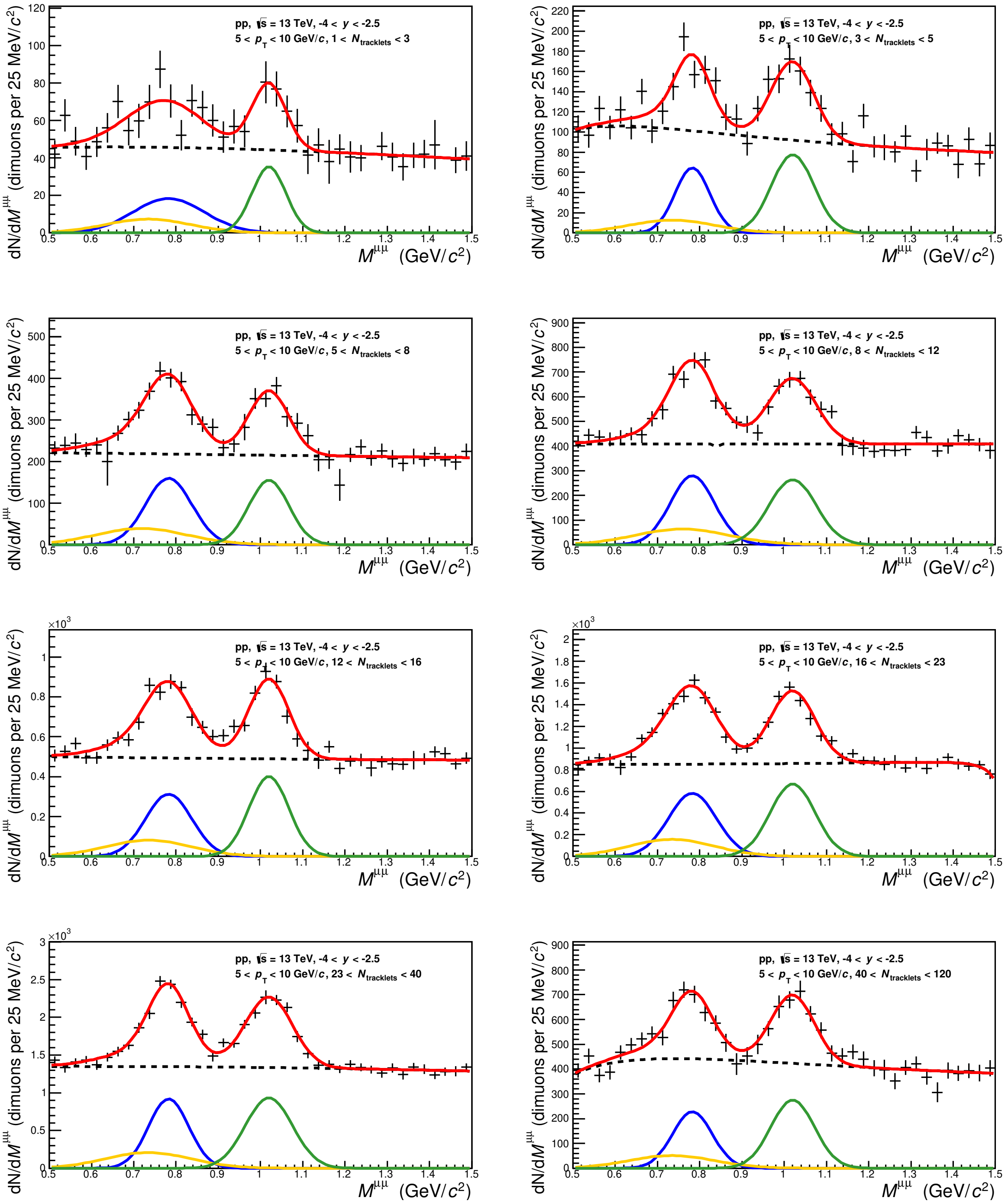

Figure 34: Unlike-sign dimuon mass spectrum subtracted uncorrelated background(histogram), inclusive function(red), ϕ meson gaussian(green), ω meson gaussian(blue), ρ meson gaussian(yellow), and VWG function in each multiplicity bin, $5 < p_{\mathrm{T}} < 10$ GeV/c.

References

[1] S. Borsanyi *et al.*, "The QCD equation of state with dynamical quarks" (2010)

[2] TAPAN K. NAYAK , "Heavy Ions: Results from the Large Hadron Collider" (2012)

[3] B. Koch *et al.*, "STRANGENESS IN RELATIVISTIC HEAVY ION COLLLISIONS" (1986)

[4] E. Andersen, *et al.*, WA97 Collaboration "Strangeness enhancement at mid-rapidity in Pb-Pb collisions at 158 A GeV/c" (1999)

[5] A. Tounsi, K. Redich, *et al.*, "Strangeness Enhancement and Canonical Suppression" (2001)

[6] A. Andronic, P. Braun-Munzinger, K. Redlich, and J. Stachel, "The thermal model on the verge of the ultimate test: particle production in Pb-Pb collisions at the LHC" (2011)

[7] P. Braun-Munzinger, J. Cleymans, H. Oescher, and K. Redlich, "Maximum Relative Strangeness Content in Heavy Ion Collisions Around 30 A·GeV" (2001)

[8] Khachatryan, V. *et al.*, CMS Collaboration "Observation of long-range near-side angular correlations in proton - proton collisions at the LHC" (2010)

[9] Khachatryan, V. *et al.*, CMS Collaboration "Evidence for collectivity in pp collisions at the LHC" (2017)

[10] The ALICE Collaboration, J. Adam *et al.*, "Enhanced production of multi-strange hadrons in high-multiplicity proton-proton collisions " (2017)

[11] V. Vislavicius, A. Kalweit, "Multiplicity dependence of light flavour hadron production at LHC energies in the strangeness canonical suppression picture" (2019)

[12] LHC ALICE J-GROUP "`http://alice-j.org`"

[13] Z.Conesa dell Valle, "Performance of the ALICE muon spectrometer . Weak boson production and measurement in heavy-ion collisions at LHC" (2007)

[14] The ALICE Collaboration, "Performance of the ALICE VZERO system" (2014)

[15] E.Botta, Proceeding of the Fifth Annual LHCP, "PARTICLE IDENTIFICATION PERFORMANCE AT ALICE" (2017)

[16] The ALICE Collaboration, " Addendum of the Letter Of Intent for the Upgrade of the ALICE Experiment : The Muon Forward Tracker " (2013)

[17] The ALICE Collaboration, B. Abelev *et al.*, "Light vector meson production in pp collisions at $\sqrt{s} = 7$ TeV " (2012)

[18] Aguilar-Benitez, M. et al., "Inclusive particle production in 400 GeV/c pp-interactions " (1991)